Stem Cell Reports
Article

ISSCR

OPEN ACCESS

iPSC-Derived Brain Endothelium Exhibits Stable, Long-Term Barrier Function in Perfused Hydrogel Scaffolds

Shannon L. Faley,[1,6] Emma H. Neal,[2,6] Jason X. Wang,[3] Allison M. Bosworth,[3] Callie M. Weber,[3] Kylie M. Balotin,[3] Ethan S. Lippmann,[2,3,4,5,7,*] and Leon M. Bellan[1,3,7,*]

[1]Department of Mechanical Engineering, Vanderbilt University, Nashville, TN 37212, USA
[2]Department of Chemical and Biomolecular Engineering, Vanderbilt University, Nashville, TN 37212, USA
[3]Department of Biomedical Engineering, Vanderbilt University, Nashville, TN 37232, USA
[4]Vanderbilt Brain Institute, Vanderbilt University Medical School, Nashville, TN 37232, USA
[5]Chemical and Physical Biology Program, Vanderbilt University, Nashville, TN 37232, USA
[6]Co-first author
[7]Co-senior author
*Correspondence: ethan.s.lippmann@vanderbilt.edu (E.S.L.), leon.bellan@vanderbilt.edu (L.M.B.)
https://doi.org/10.1016/j.stemcr.2019.01.009

SUMMARY

There is a profound need for functional, biomimetic *in vitro* tissue constructs of the human blood-brain barrier and neurovascular unit (NVU) to model diseases and identify therapeutic interventions. Here, we show that induced pluripotent stem cell (iPSC)-derived human brain microvascular endothelial cells (BMECs) exhibit robust barrier functionality when cultured in 3D channels within gelatin hydrogels. We determined that BMECs cultured in 3D under perfusion conditions were 10–100 times less permeable to sodium fluorescein, 3 kDa dextran, and albumin relative to human umbilical vein endothelial cell and human dermal microvascular endothelial cell controls, and the BMECs maintained barrier function for up to 21 days. Analysis of cell-cell junctions revealed expression patterns supporting barrier formation. Finally, efflux transporter activity was maintained over 3 weeks of perfused culture. Taken together, this work lays the foundation for development of a representative 3D *in vitro* model of the human NVU constructed from iPSCs.

INTRODUCTION

The neurovascular unit (NVU), composed of brain microvascular endothelial cells (BMECs) that form the blood-brain barrier (BBB), pericytes, neurons, and glial cells, tightly regulates transport of substances between the bloodstream and the brain. Abnormal BBB and NVU function is associated with a broad spectrum of neurological pathologies (Sweeney et al., 2018), and increasing evidence suggests that a number of non-neural disorders, such as diabetes (Prasad et al., 2014), are associated with compromised BBB integrity and/or functionality, often giving rise to secondary complications and cumulative neurological insults that increase the risk of additional neurodegenerative and cerebrovascular disease. Animal models (*in vitro* and *in vivo*) have historically been the gold-standard platform for investigating the complexities of human neurovascular disease. However, the difficulties in translating information gleaned from animal models to successful clinical intervention, which are exemplified by the lack of therapeutics that can effectively treat neurodegenerative diseases, highlight the need to develop a functional *in vitro* tissue model of the human NVU that will improve mechanistic understanding of disease progression and accelerate the development of new treatment strategies.

Recent advances in biomaterials patterning and microfluidic device fabrication have enabled a shift from standard 2D monolayer cell culture to 3D approaches that either seed cells on the surface of porous scaffolds or embed cells within hydrogel matrices. This shift has highlighted the fact that 3D culture techniques generally result in cell behavior that more closely mimics *in vivo* phenotypes (Huh et al., 2011; Ravi et al., 2015; Wikswo, 2014). Approaches that rely on cell-laden hydrogels are particularly attractive, as hydrogels mimic many aspects of the natural extracellular matrix (ECM) including stiffness, enzymatic degradability, and (with appropriate material choice or RGD modification) binding sites (Tibbitt and Anseth, 2009). Cell-laden hydrogels cast with thicknesses in the few hundred-micron range have allowed researchers to observe cell behavior in a more biomimetic, 3D environment. Additionally, cell-laden hydrogels can be patterned so that channels supporting fluid flow exist within the gel. Initial work in this area leveraged photolithographic and soft templating techniques (Cabodi et al., 2005; Golden and Tien, 2007; Zheng et al., 2012), and more recently many researchers have moved toward using 3D printing approaches to pattern either the gel itself or a sacrificial template that is first embedded within the gel and subsequently removed to form a channel (Bertassoni et al., 2014; Kolesky et al., 2014; Miller et al., 2012). While these approaches are still generally limited to forming channels with diameters on the 100-μm or larger scale, this advance enables new investigations into phenomena occurring within and around arteriole and larger-sized vessels. These platforms allow variation of multiple critical

This is an open access article under the CC BY-NC-ND license (http://creativecommons.org/licenses/by-nc-nd/4.0/).

parameters, such as flow, shear, pressure, and soluble biochemical concentration, in a 3D geometry that mimics a natural vessel.

Accordingly, several reports have implemented advanced fabrication methods to develop more complex *in vitro* BBB and NVU models. Thin-film, synthetic polyethylene glycol hydrogels supporting self-assembled NVU constructs have been used for high-throughput toxicity screening (Barry et al., 2017; Pellett et al., 2015). Meanwhile, microfluidic approaches have enabled the observation and measurement of NVU function in a highly controlled, perfused environment; these range from the commercially available sym-bbb (Prabhakarpandian et al., 2013) to highly complex, organ-on-a-chip platforms that provide powerful methods for gaining critical insights into population-specific responses to environmental perturbations with multiple readout mechanisms (Brown et al., 2015; Markov et al., 2012). While there are some recent reports that have incorporated hydrogel matrices into microfluidic devices (Kim et al., 2013; Phan et al., 2017), most of these models rely on the use of solid substrates such as polydimethylsiloxane (PDMS) or glass (Cho et al., 2015). Such BBB models are well suited to high-throughput, massively parallel drug screening efforts. However, scaffolds should ideally be more biomimetic, such that the scale, biological matrix, cellular components, and organization better approximate physiological processes, including both direct and indirect cellular interactions. Of late there have only been a few studies involving tissue-scale biological scaffolds with 3D cultures of endothelial cells (Ingram et al., 2016; Jiménez-Torres et al., 2016).

Indeed, cell fidelity has often been a limiting factor for recreating the BBB portion of NVU models. Historically, BMECs have been isolated from primary animal sources (Helms et al., 2016) but, as described above, species differences can limit the predictive power of such non-human models (Deo et al., 2013). However, BMECs from primary human sources are tedious to isolate, genetically heterogeneous between donors, can only be obtained in low yield, and often come from unhealthy tissue (e.g., brain tumor resections). Conversely, immortalized human BMECs can be obtained in high yields from a clonal source but suffer from poor passive barrier properties that do not appropriately mimic the *in vivo* BBB (Weksler et al., 2005). In recent years, the development of protocols to differentiate human induced pluripotent stem cells (iPSCs) into BMECs has circumvented many of these issues. iPSC-derived BMECs were initially characterized by expression of representative BBB markers, active efflux transporter activity, permeability to a panel of small molecules that correlate with *in vivo* uptake in rodents, and modest barrier properties as determined by transendothelial electrical resistance (TEER) measurements of ~800 Ωcm^2 (Lippmann et al., 2012). Subsequently, retinoic acid (RA) was shown to boost the passive barrier properties of iPSC-derived BMECs above 3,000 Ωcm^2 (Lippmann et al., 2014). Since these initial publications, others have validated the fidelity of these cells and advancements have been made toward improving the differentiation procedure (Appelt-Menzel et al., 2017; Hollmann et al., 2017; Katt et al., 2016; Wilson et al., 2015). In addition, these iPSC-derived BMECs, co-cultured with astrocytes on opposite sides of a Transwell filter, have been incorporated into a microfluidic device that maintained BBB properties over 10 days (Wang et al., 2017). However, studies of iPSC-derived BMEC performance in biomimetic 3D hydrogel scaffolds, which are a crucial step toward building representative *in vivo*-like NVU models that can be used for disease modeling and pre-clinical validation of drug efficacies, have been limited.

Ideally, a 3D NVU model constructed from iPSCs would be fully isogenic from a single pluripotent source, exhibit robust BBB function (including passive and active barrier properties), possess long-term stability, and be relatively simple to fabricate and implement. Herein, we describe a process to fabricate such a model, with a focus on establishing a functional iPSC-derived BMEC layer within a continuously perfused channel. Using easily accessible materials (unmodified, enzymatically crosslinked porcine gelatin) and a straightforward fabrication approach to assemble a platform that recirculates liquid through a single channel (Figures 1A–1C), we demonstrate that iPSC-derived BMECs assembled in 3D establish a robust barrier that remains stable for up to 3 weeks under continuous perfusion. Furthermore, we found that BMECs in perfused channels retain efflux transporter activity, a key functional characteristic of BBB endothelium, for over 2 weeks in culture. Together, these results validate the performance of a 3D, continuously perfused biomimetic model of brain microvasculature with long-term functional barrier properties.

RESULTS

Optimization of the Hydrogel Scaffold for Endothelial Adhesion

We first optimized scaffold composition and determined that iPSC-derived BMECs performed best when seeded on gelatin hydrogels coated with collagen IV and fibronectin (Figure S1), an approach determined to be effective in previously published protocols (Hollmann et al., 2017; Lippmann et al., 2014). With our intention to incorporate glial and neural cells in future NVU models, we initially explored fabricating the scaffolds using alginate/gelatin composite hydrogels based upon previous reports in the literature characterizing 3D culture of neural and glial cells

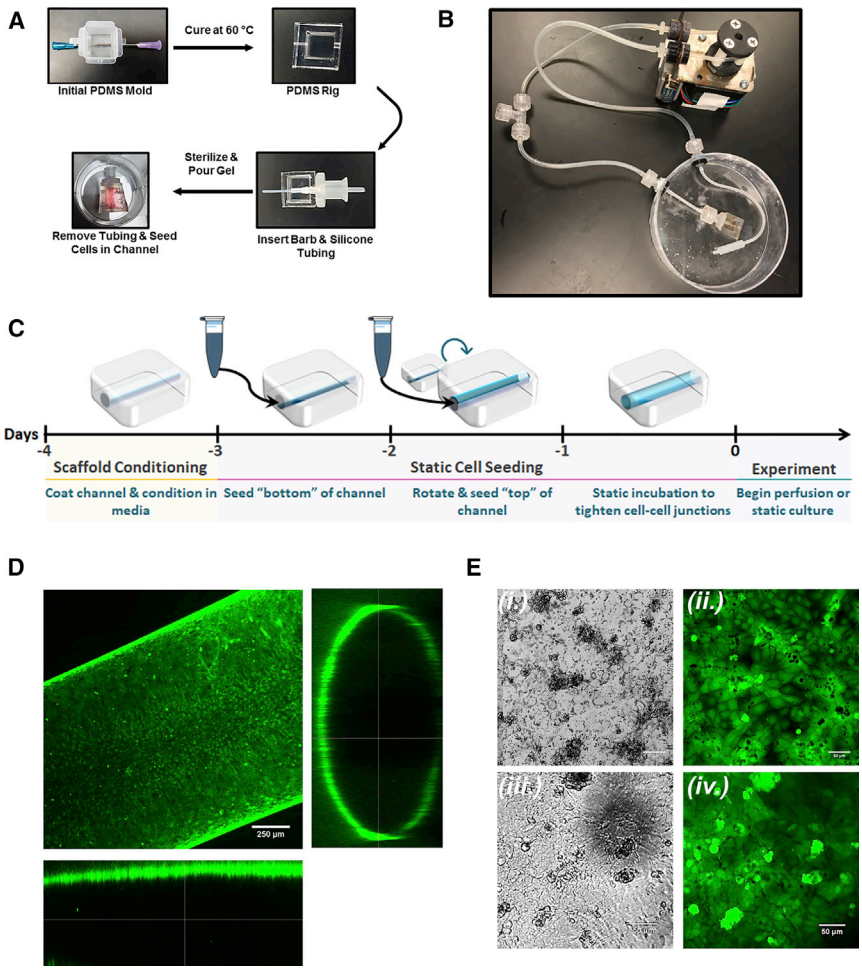

Figure 1. Cell-Laden Scaffold Assembly and Perfusion

(A and B) Fabrication of gelatin channel within supportive PDMS rig (A) and fully assembled perfusion platform (B).

(C) Schematic for cell seeding and initiation of experiments.

(D) BMECs stained with Calcein AM Ester following 7 days of culture on the channel surface as shown by orthogonal confocal image.

(E) Morphology comparison between Calcein AM-stained BMECs cultured in 2D tissue-culture plates (i and ii) and in gelatin channels (iii and iv).

(Bozza et al., 2014). We evaluated the ability of IMR90-4-derived BMECs to adhere to the surface of tissue-culture plates coated with thin hydrogel films comprising 10% gelatin or 10% gelatin/0.25% alginate composite hydrogels both with and without subsequent adsorption of the collagen/fibronectin solution commonly used in iPSC-derived BMEC cultures (Lippmann et al., 2012). As shown in Figure S1A, visual inspection of cells 24 h after seeding revealed that iPSC-derived BMECs failed to attach and grow on hydrogels containing alginate, even with additional treatment with collagen/fibronectin. Although visually indistinguishable in terms of cell morphology and viability, TEER measurements of BMECs grown on gelatin hydrogels with and without additional collagen/fibronectin coating demonstrated that gelatin treated with these additional ECM proteins yielded enhanced barrier properties (Figure S1B). Thus, we elected to proceed with all experiments using scaffolds composed of 10% gelatin and channel surfaces coated with collagen/fibronectin solution 24 h prior to cell seeding. Visual comparison of IMR90-4-derived BMECs indicates that cell morphology remains unchanged in the transition from 2D to 3D culture formats (Figures 1D and 1E).

iPSC-Derived BMECs Exhibit Robust, Long-Term Passive Barrier Function in 3D Culture

To evaluate the ability of iPSC-derived BMECs to recapitulate passive barrier function in 3D culture over the course of at least 2 weeks, we measured and compared the diffusive permeability of sodium fluorescein (molecular weight [MW] = 330 Da), 3 kDa MW dextran, and albumin (MW = 66 kDa) with human umbilical vein endothelial cells (HUVECs) and human dermal microvascular endothelial cells (μVas). The use of these tracers was intended to assess permeability to relatively small-, medium-, and large-sized molecules. In each cellular cohort, we compared samples cultured under static conditions versus continuous perfusion (100 μL/min). Results from these experiments are summarized in Figures 2 and 3, with all raw data located in Figure S2. Videos of select experiments are also provided to illustrate real-time differences in compound extravasation (Videos S1, S2, S3, and S4).

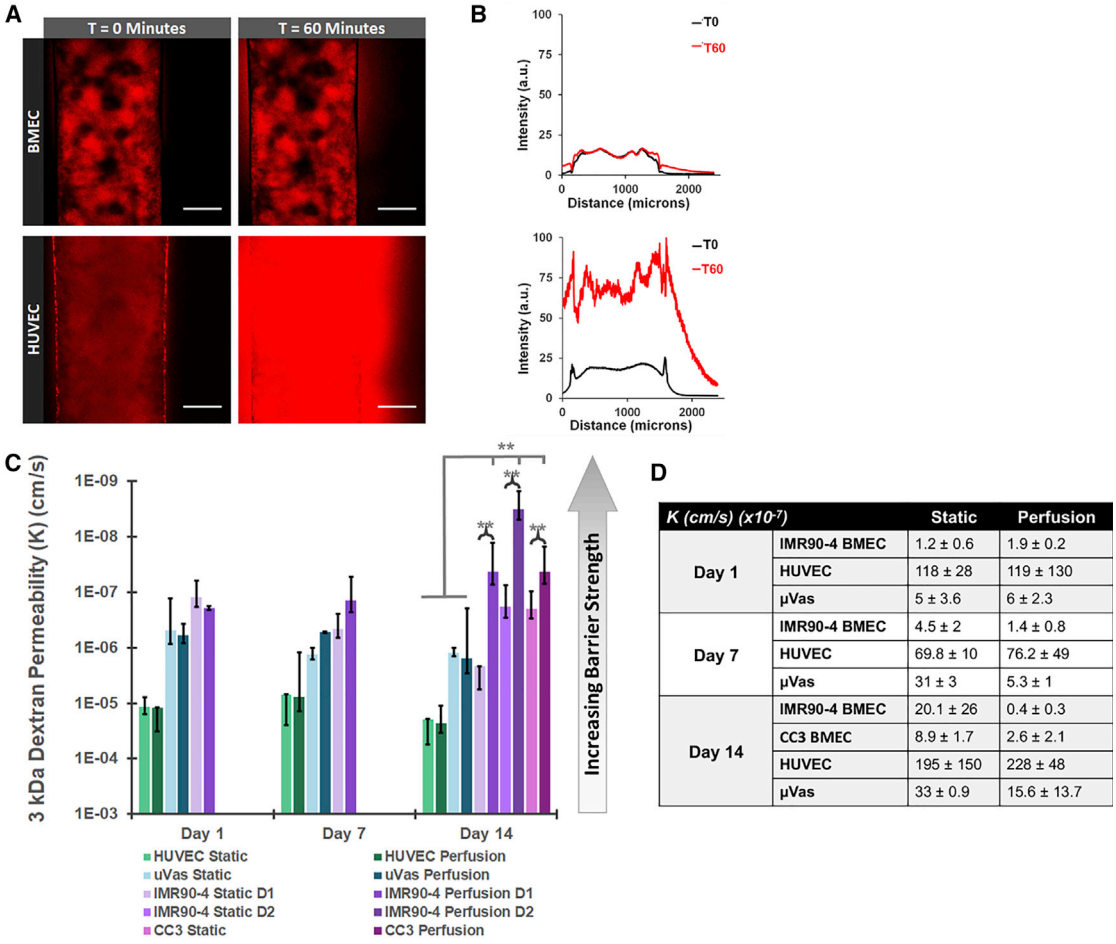

K (cm/s) (x10^{-7})		Static	Perfusion
Day 1	IMR90-4 BMEC	1.2 ± 0.6	1.9 ± 0.2
	HUVEC	118 ± 28	119 ± 130
	μVas	5 ± 3.6	6 ± 2.3
Day 7	IMR90-4 BMEC	4.5 ± 2	1.4 ± 0.8
	HUVEC	69.8 ± 10	76.2 ± 49
	μVas	31 ± 3	5.3 ± 1
Day 14	IMR90-4 BMEC	20.1 ± 26	0.4 ± 0.3
	CC3 BMEC	8.9 ± 1.7	2.6 ± 2.1
	HUVEC	195 ± 150	228 ± 48
	μVas	33 ± 0.9	15.6 ± 13.7

Figure 2. Quantitative Comparison of Cell Monolayer Permeability in Perfused and Non-perfused Channels

(A) Confocal images of 3 kDa dextran (Red) diffusion in gelatin channels lined with either iPSC-derived BMECs or HUVECs. Images show samples cultured for 7 days under static conditions. Scale bars, 100 μm.

(B) Intensity profiles across channels lined with BMECs (top) or HUVECs (bottom) at 0 and 60 min of perfusion with 3 kDa dextran.

(C and D) Graphical depiction of permeability to 3 kDa dextran on days 1, 7, and 14 of culture under either static culture or continuous perfusion at 100 μL/min (C). Average permeability coefficients are listed in (D). Data are compiled from at least eight separate channel seedings, composed of cells obtained from five independent differentiations. N ≥ 3 independent biological replicates for all data points. Error bars indicate ±1 SD. *p < 0.05, **p < 0.01 based on one-way ANOVA. Individual values from each replicate (e.g., measurements from individual devices) are listed in Figure S2.

We initially examined the permeability of 3 kDa dextran in static versus perfused channels on days 1, 7, and 14 of culture (Figures 2A–2D). The permeability coefficients for 3 kDa dextran in IMR90-4-derived BMECs were measured at nearly 2 orders of magnitude lower than HUVECs on day 1 static (K_{BMEC} = 1.2 × 10^{-7} cm/s, K_{HUVEC} = 1.2 × 10^{-5} cm/s) and perfused (K_{BMEC} = 1.9 × 10^{-7} cm/s, K_{HUVEC} = 1.2 × 10^{-5} cm/s) samples and roughly 5-fold lower than μVas ($K_{\mu Vas}$ = 5 × 10^{-7} cm/s) (e.g., the BMECs exhibit a >100-fold and 5-fold stronger passive barrier compared with HUVECs and μVas, respectively). These data indicate that the BMECs not only attach to the gelatin matrix, but also immediately form a robust barrier that is tighter than the non-BBB endothelial cells. In static culture, BMEC barrier function declined on day 7 (K_{BMEC} = 4.6 × 10^{-7} cm/s) and day 14 (K_{BMEC} = 2.2 × 10^{-6} cm/s), although it remained ~10-fold better than HUVEC (K_{HUVEC} = 7 × 10^{-6} cm/s and 2 × 10^{-5} cm/s on days 7 and 14, respectively) and μVas controls ($K_{\mu Vas}$ = 1.3 × 10^{-6} cm/s and 1.2 × 10^{-6} cm/s on days 7 and 14, respectively). In contrast, the barrier against 3 kDa dextran in BMECs that were continuously perfused for 2 weeks was comparable with initial values (K_{BMEC} = 4.3 × 10^{-8} cm/s on day 14), suggesting that exposure to shear might further

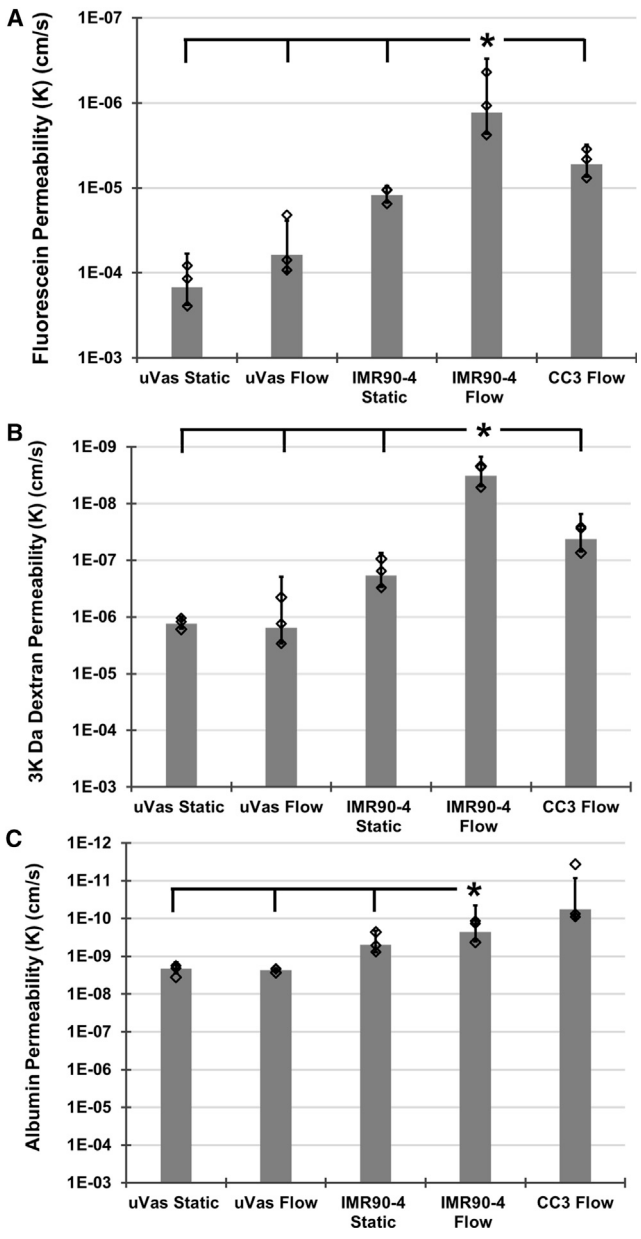

Figure 3. Permeability Coefficients for Molecules of Varying Molecular Weights

Comparison of permeability for (A) sodium fluorescein, (B) 3 kDa dextran, and (C) albumin between μVas, IMR90-4-derived BMECs, and CC3-derived BMECs that were maintained under either static conditions or continual perfusion for 14 days. Diamonds indicate actual values of individual replicates. N ≥ 3 independent biological replicates for all data points. Error bars indicate ±1 SD. *p < 0.05 based on one-way ANOVA.

stabilize, and perhaps enhance, BMEC barrier integrity over time. A similar trend was observed in μVas ($K_{\mu Vas}$ = 1.5 × 10^{-6} cm/s on day 14), although the permeability coefficient for these cells remained more than ten times greater than BMECs. We also separated data compiled from different IMR90-4 BMECs differentiations to show biological reproducibility (all data from Figures 2 and 3 are compiled from more than five independent differentiations). The permeability to 3 kDa dextran from two separate IMR90-4 BMEC differentiations (indicated as either D1 or D2) were measured at day 14 under both static and perfused conditions. All BMEC cohorts exhibit permeability coefficients over 10-fold smaller than those for HUVEC/μVas controls. Furthermore, all BMECs under perfusion are significantly less permeable than their non-perfused counterparts, further highlighting the reproducibility of the system.

To further explore the influence of perfusion upon barrier strength in BMECs, we measured the diffusion coefficients of sodium fluorescein and albumin in addition to 3 kDa dextran after 14 days of perfused or static culture (Figure 3). To validate these results in a different iPSC line, we also measured permeability in CC3-derived BMECs (Hollmann et al., 2017) (Figures 2 and 3). Both IMR90-4- and CC3-derived BMECs subjected to perfusion for 14 days exhibited permeability to all compounds that was an order of magnitude lower than μVas controls. Additionally, IMR90-4-derived BMECs subjected to perfusion exhibited permeability that was significantly lower compared with non-perfused counterparts, confirming permeability trends across a spectrum of molecular weights. Exclusion of albumin suggests reduced vesicular transport, which is a hallmark of the BBB. To further probe this finding, we used qPCR to quantify *MFSD2A* and *CAV1* (caveolin-1) expression. *MFSD2A*, which is highly expressed in brain endothelium relative to lung and liver endothelium and known to suppress endocytosis/transcytosis (Ben-Zvi et al., 2014), was not expressed at significantly different levels between BMECs and μVas (Figure S3). However, *CAV1*, an important component of vesicular transport that is suppressed in BMECs and activated under pathogenic conditions such as ischemia/reperfusion (Knowland et al., 2014), exhibited ~8-fold higher expression in μVas relative to BMECs. Coupled with the permeability data demonstrating reduced albumin extravasation, these data suggest the BMECs suppress vesicular transport, although not necessarily through *MFSD2A* upregulation. Since these BMECs are maintained in isolation, it is possible that regulatory cues for *MFSD2A* provided by other cell types (e.g., pericytes) are not present. In future model iterations, inclusion of these cell types could further suppress vesicular transport.

To further examine gene expression patterns, we used qPCR to quantify *OCLN* (occludin) and *SLC2A1* (GLUT-1) between IMR90-4-derived BMECs and μVas at day 14 under perfusion. *OCLN* and *SLC2A1* are recognized as being relatively specific to BBB compared with peripheral

endothelium (Daneman and Prat, 2015), and these genes were expressed at ~5-fold and ~11-fold higher levels, respectively, in BMECs (Figure S3). Next, we used RNA sequencing to compare global gene expression patterns in BMECs cultured for 1 day under static conditions and 14 days under constant perfusion (Table S1). The Pearson correlation coefficient between these samples was 0.91, which indicates a strong positive association and provides evidence that the BMEC gene expression signatures are maintained under longitudinal perfusion.

Finally, to establish appropriate correlations between 2D and 3D barrier function, we performed a similar dextran diffusion assay using CC3-derived BMECs and HUVECs cultured in Transwell filters (Figure S4A). Permeability values obtained from cells cultured in 2D were on the same order of magnitude as those obtained in 3D channels (10^{-7} cm/s for BMECs and 10^{-5} cm/s for HUVECs), thus validating the measurements made within the tissue construct. Interestingly, permeability values for both BMECs and HUVECs remained stable over time in 2D, unlike the steady increase in permeability observed in cells lining non-perfused channels, indicating a possible role for nutrient exchange in maintaining barrier integrity in the 3D construct. To further explore this potential impact of nutrient exchange, we examined the permeability in BMECs and μVas in 3D culture under stop-flow conditions, in which samples were subjected to perfusion from the medium reservoir, but for only 10 min per day; these experiments permitted nutrient exchange with minimal exposure to shear stress (we note that the scaffolds are designed such that the upper surface of the hydrogel is in direct contact with the medium reservoir, which likely provides some additional material exchange to the cells). Results from these stop-flow experiments revealed that permeability was similar to, and in some cases worse than, static conditions, suggesting that fluidic shear stress does maintain barrier integrity within the context of the 3D culture platform (Figure S4B). We note the possibility that the endothelial cells provide greater conditioning of the medium in the Transwell system relative to the hydrogel system due to volume differences (2 mL versus ~40 mL), and that shear stress-induced effects may compensate for these trophic factors in the perfusion versus static conditions. However, because the goal of this work is to solely establish the performance of the 3D BBB culture platform, these mechanisms were not explored further.

Assessment of Junctional Integrity

To validate that the observed permeability values corresponded to proper cell-cell junction formation, we evaluated cells for junctional and cytoskeletal markers including occludin, claudin-5, VE-cadherin, and F-actin. CC3-derived BMECs lining gelatin channels show robust expression of both occludin and claudin-5 localized to intercellular junctions (Figure 4A). F-actin expression (Figure 4B) similarly indicated strong intercellular localization in BMEC-lined channels. In addition, F-actin staining patterns demonstrate the lack of cellular elongation in cells exposed to fluidic shear, a property previously reported to be a unique characteristic of BMECs (DeStefano et al., 2017; Reinitz et al., 2015; Wang et al., 2017; Ye et al., 2014). This is particularly evident when BMEC morphology is compared with HUVECs and μVas maintained under static (Figure 4C) and perfused (Figure 4D) conditions. HUVECs and μVas also strongly expressed VE-cadherin along cell boundaries, but claudin-5 expression was generally absent at cell boundaries and instead diffusely distributed within the cells. Claudin-5 is essential for tight junction formation and regulation of BBB permeability, particularly to small compounds (Nitta et al., 2003). In contrast, claudin-5 is functionally insignificant in establishment of an umbilical vein (HUVEC) barrier (Kluger et al., 2013). When compared with the fluorescein permeability data (Figure 3), these overall data strongly suggest the formation of robust cell-cell junctions in BMECs in 3D culture.

Influence of Increased Shear Stress on Barrier Function

Based on the comparisons between perfusion, static, and stop-flow permeability experiments, we sought to further probe the effects of shear stress on barrier integrity. We found that permeability in channels perfused at 100 μL/min heterogeneously declined between two samples by day 21 (Figure 5A). One sample exhibited substantially worse permeability of 2.4×10^{-6} cm/s, while the other sample remained extremely tight at 5.8×10^{-8} cm/s. At this time, we observed signs of angiogenic sprouting at 21 days of perfusion (Figure 5C), which was not evident in previous time points in either static or perfused samples and could explain the decline in barrier function between samples.

Perfusion of the ~800-μm diameter channel at a rate of 100 μL/min generates a wall shear of approximately 32 mPa (0.3 dyne/cm^2), well below the physiological range of ~1–3 Pa (10–30 dyne/cm^2) estimated for brain microvasculature (Cheng et al., 2007; Cucullo et al., 2008; Garcia-Polite et al., 2017; Koutsiaris et al., 2013). Compared with the permeability of BMECs perfused at 100 μL/min, perfusion at 300 μL/min and 1,000 μL/min (wall shear of approximately 100 mPa [1 dyne/cm^2] and 320 mPa [3.2 dyne/cm^2], respectively) for 14 days yielded an overall reduction in passive barrier function. As shown in Figure 5B, the permeability coefficient to 3 kDa dextran for BMECs perfused at 300 μL/min and 1,000 μL/min was 2.9×10^{-7} cm/s and 4.8×10^{-7} cm/s, respectively, which is approximately ten times more permeable than BMECs perfused at 100 μL/min. This increase in permeability also corresponded to an increase in observed incidence of

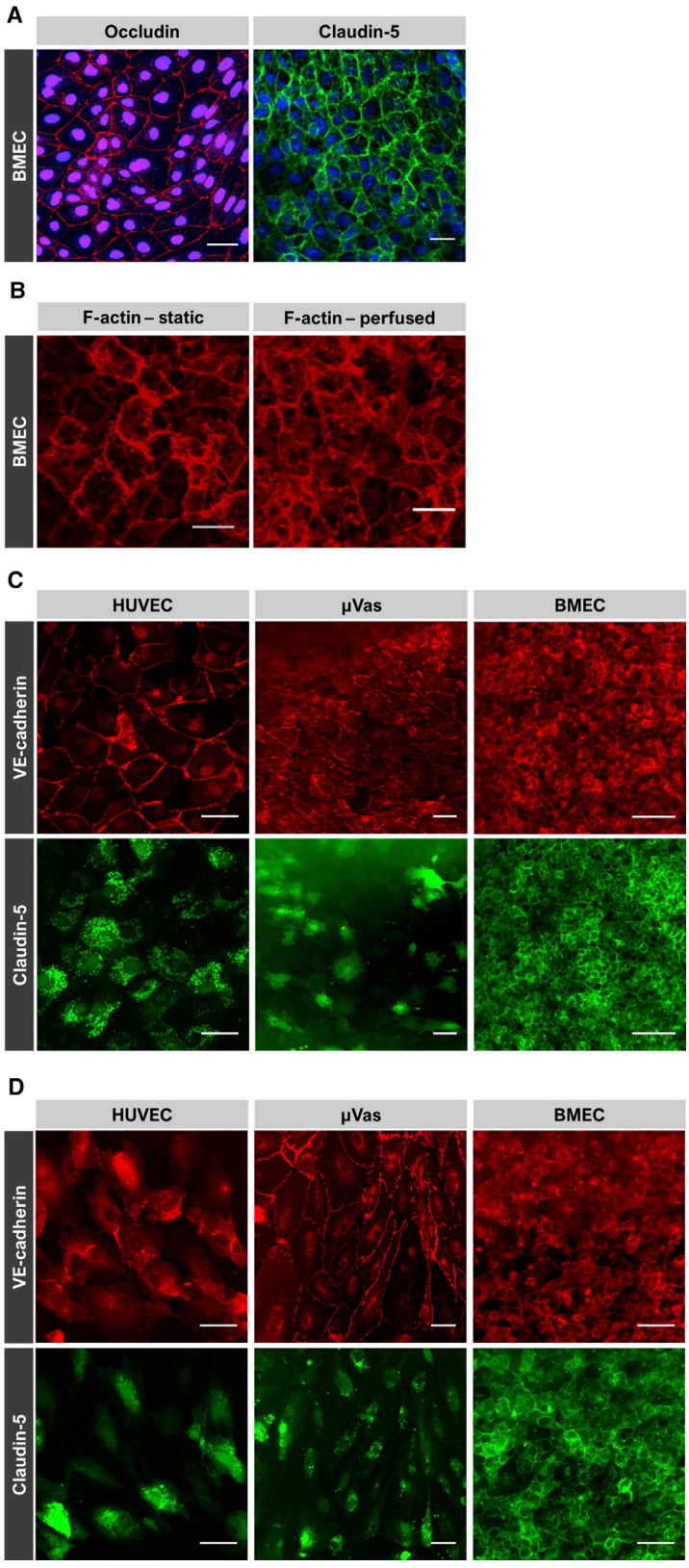

Figure 4. Immunofluorescent Staining

(A) IMR90-4-derived BMECs labeled for occludin and claudin-5 at day 1 under static conditions. Nuclei are counterstained with Hoechst.

(B) IMR90-4-derived BMECs labeled for F-actin at day 1 under static conditions and day 14 under perfused conditions.

(C and D) HUVECs, μVas, and IMR90-4-derived BMECs labeled for VE-cadherin and claudin-5 at day 7 under static (C) and perfused (D) conditions. Each individual image reflects a summative z projection of individual confocal images without additional processing to flatten images. For each fluorescence channel, the intensity scale is held constant across all samples. As a result, in some images there is a perceived decrease in fluorescence signal for points farthest from the objective that is reflective of channel curvature and slight variations in gelatin topology rather than inherent signal.

Scale bars, 50 μm.

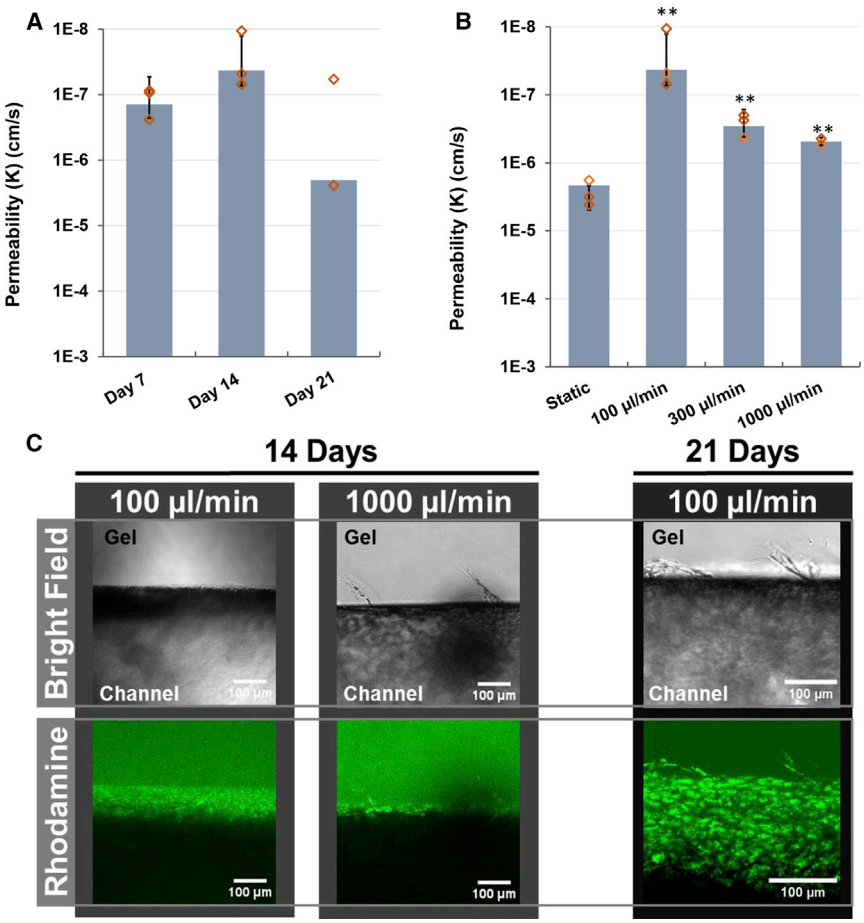

Figure 5. Relative Impact of Shear on BMEC Permeability

(A) Permeability to 3 kDa dextran in IMR90-4-derived BMECs perfused at 100 µL/min over 21 days. N ≥ 3 independent biological replicates for all datasets, except N = 2 independent biological replicates for the day-21 time point. Diamonds indicate actual values of individual replicates. Error bars indicate ±1 SD.

(B) Permeability coefficients to 3 kDa dextran in BMECs perfused for 14 days at 100, 300, and 1,000 µL/min, compared with the static control. Diamonds indicate actual values of individual replicates. N = 2 independent biological replicates for 1,000 µL/min dataset, N ≥ 3 independent biological replicates for all other cohorts. Error bars indicates ±1 SD. **p < 0.01 compared with static based upon one-way ANOVA.

(C) Images showing cell sprouting in channels perfused for 14 days (left) at 100 and 1,000 µL/min, and 21 days (right) at 100 µL/min. Top image is bright-field, bottom image shows cells stained by rhodamine 123.

angiogenic sprouting observed on day 14 in channels perfused at higher flow rates and day 21 in channels perfused at 100 µL/min (Figure 5C). Importantly, these values are still 10-fold lower than BMECs maintained under static conditions, providing additional evidence that perfusion, even at subphysiological levels of shear, stabilizes barrier function over time despite minor vascular sprouting.

Assessment of Active Barrier Function

As discussed previously, a hallmark of brain endothelium is the expression of active efflux transporter such as P-glycoprotein (Pgp), breast cancer resistance protein, and multidrug resistance proteins (MRPs). Accordingly, numerous reports have demonstrated that iPSC-derived BMECs possess active efflux activity determined by substrate inhibition assays (Hollmann et al., 2017; Lippmann et al., 2012, 2014). Here, we sought to characterize this efflux activity in IMR90-4-derived BMECs under 3D perfusion culture. Intracellular accumulation of rhodamine 123 (a Pgp substrate) was evaluated in the presence or absence of cyclosporin A (a Pgp inhibitor) in BMECs after 14 days of perfusion. Similarly, MRP-associated efflux activity was assessed by measuring intracellular accumulation of H2DCFDA in the presence or absence of inhibitor MK-571. As shown in Figures 6A and 6B, BMECs possess robust Pgp activity after 14 days in culture as determined by an increase in intracellular fluorescence of inhibited samples exceeding 80%, providing supporting evidence of the long-term functionality of iPSC-derived BMECs in this 3D culture format. Pgp activity was not influenced by perfusion rate (100, 300, or 1,000 µL/min) and remained stable at 21 days of perfusion at 100 µL/min. Comparatively, µVas also exhibited increased uptake of rhodamine 123 and H2DCFDA in the presence of inhibitors (Figure 6C). However, uptake was significantly lower than for BMECs, likely indicating that BMECs have a higher efflux activity and/or expression of efflux transporters. Although peripheral endothelial cells are not commonly known for possessing efflux activity, Pgp expression has historically been observed in skin endothelial cells from papillary but not reticular dermis (Cordon-Cardo et al., 1989). Thus, some baseline efflux activity may reflect the source of these control cells.

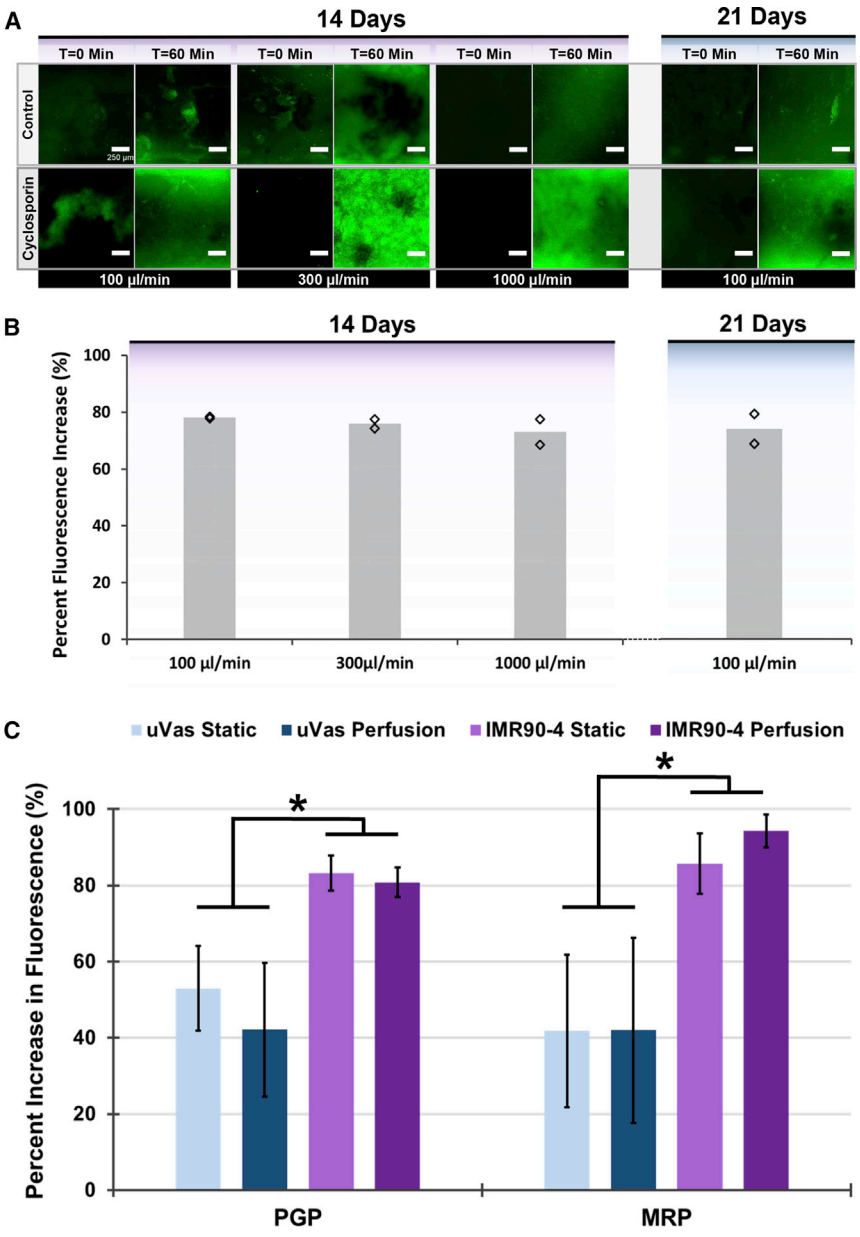

Figure 6. Assessment of Efflux Transporter Activity Reflects Long-Term BMEC Functionality in Perfused Channels

(A) Confocal images (z projections) of IMR90-4-derived BMECs after 14 and 21 days of perfusion at various flow rates that were imaged over the course of 1 h of perfusion with medium containing rhodamine 123 alone (control; top row) or following a 1-h pre-incubation with cyclosporin A (bottom row). Each pair of control versus cyclosporin A comparisons were conducted using separate channel devices from the same seeding and perfusion cohort. Images reflect summative z projections of confocal z stacks without any further processing to flatten images, and all images are presented using the same intensity scale.

(B) The increase in cellular rhodamine 123 accumulation resulting from Pgp inhibition is quantified in terms of cellular fluorescence intensity relative to non-inhibited controls. $N \geq 2$ independent biological replicates for each dataset. Diamonds indicate actual values of individual replicates.

(C) Comparison of Pgp and MRP activity in channels lined with either µVas or BMECs after 14 days of culture. $N \geq 3$ independent biological replicates for each dataset. Error bars indicate ±1 SD. *$p < 0.05$ based on one-way ANOVA.

DISCUSSION

In this study, we demonstrate the capability of iPSC-derived BMECs to form confluent 3D monolayers that sustain barrier integrity for up to 3 weeks under continuous perfusion, as measured by low passive diffusion to a cohort of molecular tracers, tight junction localization, and efflux transporter activity. Overall, two of the most significant findings in this work are the longevity of BMEC barrier function and relative barrier properties compared with the non-BBB controls, particularly with respect to permeability of low molecular weight compounds. We note that relative to µVas, iPSC-derived BMECs were significantly less permeable to fluorescein, which is an important small-molecule tracer for qualifying BBB integrity. The absolute permeability of fluorescein is similar to results obtained from measurements in 2D Transwell platforms (10^{-6}–10^{-7} cm/s) (Hollmann et al., 2017), indicating consistency in BMEC performance and robustness of the paracellular barrier in 3D culture. Meanwhile, the exclusion of albumin and decreased *CAV1* expression suggest reduced vesicular transport in BMECs relative to non-BBB controls.

We further note that perfusion of BMEC-lined channels under low shear conditions has a stabilizing effect on barrier integrity over time compared with non-perfused controls, with similar performance in barrier function in

BMECs derived from two separate iPSC lines. Our data indicate that perfusion helps maintain long-term barrier function through a combined effect of shear-induced mechanical cues and continual medium circulation providing improved nutrient/waste exchange. Recently, iPSC-derived BMECs co-cultured with astrocytes in perfused microfluidic channels were reported to maintain *in vivo*-like TEER values for 12 days, whereby the authors concluded that shear forces were not essential for the establishment of strong intercellular junctions but did provide a clear stabilizing effect upon barrier integrity over time (Wang et al., 2017), which is consistent with our findings. Another group has reported that shear forces are non-requisite for tight junction formation in iPSC-derived BMEC monolayers, but that shear positively contributes to barrier health by providing necessary mechanical cues as well as reducing reactive oxygen species-mediated degradation (DeStefano et al., 2017; Rochfort et al., 2015). In our 3D system, increased shear forces above our initially tested values did not strengthen or stabilize barrier function. However, these measurements are complicated by the observation of increased angiogenic sprouting at earlier time points associated with higher flow rates, and the cytoskeletal restructuring of angiogenic sprouting is known to increase the permeability of brain endothelium (Kutys and Chen, 2016). It is likely that the increase in interstitial flow associated with higher perfusion rates resulted in increased sprouting in BMEC monolayers, a process normally inhibited by interactions with surrounding smooth muscle cells and astrocytes (Galie et al., 2014; Partyka et al., 2017). Thus, we hypothesize that incorporation of additional NVU cell types will further stabilize barrier function by preventing angiogenic sprouting, which will be examined in future studies.

Interestingly, despite robust barrier function and expression of junction-associated VE-cadherin, claudin-5, and occludin protein, our global expression data indicate low mRNA transcript abundance for both endothelial and BBB-associated genes. Transcript levels in iPSC-derived BMECs cultured for 1 day under static conditions were similar to iPSC-derived BMECs cultured in 2D well plates (Qian et al., 2017), suggesting consistency with other models. We note that transcriptional profiling has been performed on both mouse and human brain endothelial cells, and for canonical BBB/endothelial genes (e.g., *OCLN*, *CLDN5*, *CDH5*, *PECAM1*, *SLC2A1*, *MFSD2A*, *ABCB1*), expression levels in mouse are consistently ~10- to ~100-fold higher than in human (Zhang et al., 2016). At present, it is unclear whether low transcript abundance in iPSC-derived BMEC models reflects *in vitro* culture conditions or a species difference, and more investigations are required in this area. We also note that despite overall similarity between day-1 static cultures and day-14 perfusion cultures, endothelial-specific genes become noticeably downregulated at the later time point. Thus, although perfusion and shear stress may help stabilize barrier function through upregulation of currently unknown signaling pathways, these factors potentially have a lower influence on maintenance of vascular identity. We hypothesize that inclusion of pericytes and future optimization of media composition will help promote maintenance of endothelial gene signatures at these later time points. These investigations and more in-depth analyses of transcript data are expected to identify more explicit differences between 2D and 3D cultures of iPSC-derived BMECs, similar to other studies (Zhang et al., 2017), as well as possible human-specific BBB gene expression signatures.

Overall, we highlight the utility of our 3D model for exploring interactions between NVU cell types, modeling neurovascular disease, and assessing treatment strategies. Since we have used gelatin with a benign enzymatic cross-linking approach compatible with cell encapsulation (Lee et al., 2016), we expect to be able to establish co-cultures that represent endogenous organization of NVU cell types. Given advancements in the production of neurovascular cells from iPSCs, including diverse subtypes of neurons, astrocytes, oligodendrocytes, microglia, pericytes, and smooth muscle, a fully isogenic 3D model is a realistic possibility in the near future. Also, given prominent vascular contributions to neurodegenerative diseases (Sweeney et al., 2018), future iterations of this biomimetic 3D NVU model could provide a useful platform for modeling disease phenotypes. Lastly, although this model is not expected to replace standard Transwell setups for screening prospective therapeutic compounds for BBB permeation, the performance of lead candidates could be further tested in these 3D NVU systems, where a more physiological microenvironment is expected to improve predictions of therapeutic efficacy.

EXPERIMENTAL PROCEDURES

Cell Culture

IMR90-4 (Yu et al., 2007) and CC3 (Kumar et al., 2014) iPSCs were maintained on growth factor-reduced Matrigel (VWR) in E8 medium (produced in-house as previously described) (Hollmann et al., 2017). iPSCs were passaged every 3–4 days with Versene (Thermo Fisher) as previously described. Differentiation to BMECs was conducted as previously described. In brief, iPSCs were passaged to single cells with Accutase (Thermo Fisher) and seeded overnight on Matrigel at a density of 12,500–15,800 cells/cm^2 in E8 medium containing 10 μM Y27632 (Tocris). The following day, cells were fed with E6 medium (produced in-house as previously described) (Hollmann et al., 2017), and medium was changed every day thereafter. On day 4, cells were switched to human endothelial serum-free medium (hESFM; Thermo Fisher)

containing 1% platelet-poor plasma-derived serum (PDS; Alfa Aesar), 20 ng/mL basic fibroblast growth factor (bFGF; Peprotech), collectively referred to as EC culture medium, and 10 μM all-*trans* RA (Sigma). On day 6, cultures were collected with Accutase and either frozen in 60% EC culture medium, 10% DMSO (Sigma), 30% fetal bovine serum (FBS; Thermo Fisher), and 10 μM Y27632 as previously described (Wilson et al., 2016), or seeded directly into scaffolds. HUVECs and μVas (Angioproteomie) were cultured in DMEM/F12 medium (Thermo Fisher) supplemented with 5% FBS (Gibco), 10 mM L-glutamine (Corning), 50 μg/mL ascorbic acid (Thermo Fisher), 0.75 U/mL heparin (Thermo Fisher), 15 ng/mL insulin growth factor 1, 5 ng/mL vascular endothelial growth factor, 5 ng/mL bFGF, and 5 ng/mL epidermal growth factor (all from Peprotech).

Scaffold Fabrication

External support frames for gelatin scaffolds were generated from thin slabs of PDMS cast in small Peel-A-Way embedding molds (Fisher Scientific) transected by two intersecting needles (gauge 23 and 16, BD Biosciences). After removing the central section and bonding to a thin PDMS film base, a barbed luer fitting (Cole Parmer) was attached to the inlet to facilitate easy integration with the fluidic apparatus. Tubing ($1/16^{th}$ inch outer diameter, VWR) threaded through the barbed inlet served as the channel mold (Figure 1A). PDMS frames (5 × 5 × 2 mm) were washed and sterilized in 70% ethanol with sonication. Sterile solution of 10% (w/v) porcine gelatin (300 bloom, Sigma) combined 10:1 (v/v) with 10% (w/v) microbial transglutaminase (Modernist Pantry) was poured into the assembled frames and allowed to polymerize in a 37°C incubator for 4 h. The channel was formed by removal of tubing and was coated with 0.4 mg/mL collagen IV (Sigma) and 0.1 mg/mL fibronectin (Sigma) and conditioned in complete medium overnight before seeding channels with 3×10^6 cells/mL of either iPSC-derived BMECs, RFP-expressing HUVECs, or μVas. The approximate volume of the channel (~800 μm × 5 mm) is 2.5 μL.

Cell Seeding

IMR90-4-derived BMECs were reconstituted from frozen stock, whereas CC3-derived BMECs, HUVECs, and μVas were seeded from live cultures. For quality control, TEER was measured across BMECs seeded concurrently in Transwell filters and was consistent with previous publications. Cells were suspended at 3×10^6 cells/mL in their standard medium and pipetted through the inlet fitting to coat the bottom half of a channel. Cells were incubated for either 4 h or overnight at 37°C to facilitate attachment. The process was then repeated to seed the top half of the channel. Cells were stained with 2 μM Calcein AM (Life Technologies) and imaged by confocal microscopy (LSM 710, Zeiss) to confirm a confluent cell layer throughout channel before connecting to perfusion (Figure 1C).

Scaffold Culture and Perfusion

On experiment day 0, hydrogels were placed in a Petri dish and either remained in static culture or were connected to a perfusion system (Figure 1B). Under both conditions, the hydrogels are submerged in ~40–45 mL of medium. Based on the design of the PDMS frame, the upper surface of each hydrogel is in direct contact with the medium. For perfusion, a custom peristaltic pump (O'Grady et al., 2018) circulated culture medium through the channel at 100 μL/min. For samples perfused at rates greater than 100 μL/min, the flow rate was increased to the indicated value following an initial 24-h perfusion at 100 μL/min. As seen in Figure 1B, medium is extracted through the open tube not connected to the hydrogel, circulated through the hydrogel, and expelled back into the bulk reservoir. HUVECs were cultured in the same medium described above, whereas BMECs and μVas were both cultured in hESFM containing 1% PDS, 10 μM RA, and 10 μM Y27632. The medium was unchanged throughout the course of each experiment. Components used to construct the perfusion system are described in Figure S5.

Permeability Measurements

Permeability was measured by imaging diffusion of 2 μM sodium fluorescein (Sigma), 12.5 μg/mL 3 kDa AF680-conjugated dextran (Thermo Fisher), and 80 μg/mL Texas red-conjugated albumin (Thermo Fisher) across cell monolayers. During the course of the imaging experiment, channels were perfused at a rate of 30 μL/min for 2 h while obtaining fluorescence images every 30 s using the LSM 710 confocal microscope with pinhole set to 1 Airy unit. The resulting image intensity profiles were processed in FIJI (Schindelin et al., 2012) using a custom macro to automate extraction of fluorescence intensity values of the channel region, the diffusion region between channel and edge, and the edge of the gel. These values were then imported into a MATLAB (Mathworks) script to calculate K (cm s^{-1}), the permeability of gelatin scaffold and cell layer combined, as detailed in Supplemental Experimental Procedures and Figure S6.

Efflux Transporter Activity Assays

Pgp activity was assessed by measuring accumulation of fluorescent dye, rhodamine 123, in samples pre-incubated with and without Pgp-specific inhibitor, cyclosporin A. MRP activity was assessed by measuring fluorescence accumulation of fluorescent dye H2DCFDA, in samples pre-incubated with and without MRP-specific inhibitor, MK-571. Specifically, non-inhibited controls were evaluated by perfusion (30 μL/min) with medium supplemented with 10 μM rhodamine 123 (Thermo Fisher) or 10 μM H2DCFDA (Thermo Fisher) and 12.5 μg/mL 3 kDa dextran. Inhibited samples were pre-incubated in medium containing 10 μM cyclosporin A (Tocris) or 10 μM MK-571 (Tocris) for 1 h, then similarly perfused with the medium supplemented with 12.5 μg/mL 3 kDa dextran and appropriate inhibitor/dye cocktail (Pgp: 10 μM cyclosporin A and 10 μM rhodamine 123; MRP: 10 μM MK-571 and 10 μM H2DCFDA). Confocal z stacks were obtained at 0 and 60 min of perfusion. For each sample, the change in intracellular fluorescence intensity was determined using FIJI by adding the cellular fluorescence from each z stack, then subtracting the cumulative fluorescence intensity of the initial z stack from the final z stack ($\Delta I = I_{final} - I_{initial}$). The percent increase in fluorescence was calculated using the formula

$$\frac{\Delta I_{inhibited} - \Delta I_{non-inhibited}}{\Delta I_{inhibited}} \times 100$$

where $\Delta I_{\text{inhibited}}$ is the change in fluorescence calculated from channels exposed to cyclosporin A and $\Delta I_{\text{non-inhibited}}$ is the change in fluorescence calculated from channels not exposed to inhibitor.

ACCESSION NUMBERS

The RNA-sequencing data referenced in this paper were submitted to GEO under accession number GEO: GSE122588.

SUPPLEMENTAL INFORMATION

Supplemental Information includes Supplemental Experimental Procedures, six figures, two appendices, one table, and four videos and can be found with this article online at https://doi.org/10.1016/j.stemcr.2019.01.009.

AUTHOR CONTRIBUTIONS

S.L.F., E.H.N., E.S.L., and L.M.B. designed experiments. S.L.F., E.H.N., A.M.B., C.M.W., K.M.B., and J.X.W. conducted/assisted with experiments and/or reagent preparation. All authors read and approved the manuscript.

ACKNOWLEDGMENTS

Funding for this research was provided by NIH 4R00EB013630 (NIBIB) (L.M.B.), NSF BMAT 1506717 (L.M.B.), a NARSAD Young Investigator Award from the Brain and Behavior Research Foundation (E.S.L.), NSF CBET 1706155 (E.S.L.), and the donors of Alzheimer's Disease Research, a program of the BrightFocus Foundation (grant A20170945 to E.S.L.). E.H.N. was supported by a National Science Foundation Graduate Research Fellowship. The authors gratefully acknowledge the SyBBURE Searle Undergraduate Research Program supporting C.M.W. and J.X.W.

Received: October 25, 2017
Revised: January 11, 2019
Accepted: January 14, 2019
Published: February 14, 2019

REFERENCES

Appelt-Menzel, A., Cubukova, A., Günther, K., Edenhofer, F., Piontek, J., Krause, G., Stüber, T., Walles, H., Neuhaus, W., and Metzger, M. (2017). Establishment of a Human blood-brain barrier co-culture model mimicking the neurovascular unit using induced pluri- and multipotent stem cells. Stem Cell Reports *8*, 894–906.

Barry, C., Schmitz, M.T., Propson, N.E., Hou, Z., Zhang, J., Nguyen, B.K., Bolin, J.M., Jiang, P., McIntosh, B.E., Probasco, M.D., et al. (2017). Uniform neural tissue models produced on synthetic hydrogels using standard culture techniques. Exp. Biol. Med. *242*, 1679–1689.

Ben-Zvi, A., Lacoste, B., Kur, E., Andreone, B.J., Mayshar, Y., Yan, H., and Gu, C. (2014). Mfsd2a is critical for the formation and function of the blood-brain barrier. Nature *509*, 507–511.

Bertassoni, L.E., Cecconi, M., Manoharan, V., Nikkhah, M., Hjortnaes, J., Cristino, A.L., Barabaschi, G., Demarchi, D., Dokmeci, M.R., Yang, Y., et al. (2014). Hydrogel bioprinted microchannel networks for vascularization of tissue engineering constructs. Lab Chip *14*, 2202–2211.

Bozza, A., Coates, E.E., Incitti, T., Ferlin, K.M., Messina, A., Menna, E., Bozzi, Y., Fisher, J.P., and Casarosa, S. (2014). Neural differentiation of pluripotent cells in 3D alginate-based cultures. Biomaterials *35*, 4636–4645.

Brown, J.A., Pensabene, V., Markov, D.A., Allwardt, V., Neely, M.D., Shi, M., Britt, C.M., Hoilett, O.S., Yang, Q., Brewer, B.M., et al. (2015). Recreating blood-brain barrier physiology and structure on chip: a novel neurovascular microfluidic bioreactor. Biomicrofluidics *9*, 054124.

Cabodi, M., Choi, N.W., Gleghorn, J.P., Lee, C.S.D., Bonassar, L.J., and Stroock, A.D. (2005). A microfluidic biomaterial. J. Am. Chem. Soc. *127*, 13788–13789.

Cheng, C., Helderman, F., Tempel, D., Segers, D., Hierck, B., Poelmann, R., van Tol, A., Duncker, D.J., Robbers-Visser, D., Ursem, N.T.C., et al. (2007). Large variations in absolute wall shear stress levels within one species and between species. Atherosclerosis *195*, 225–235.

Cho, H., Seo, J.H., Wong, K.H.K., Terasaki, Y., Park, J., Bong, K., Arai, K., Lo, E.H., and Irimia, D. (2015). Three-dimensional blood-brain barrier model for *in vitro* studies of neurovascular pathology. Sci. Rep. *5*, 15222.

Cordon-Cardo, C., O'Brien, J.P., Casals, D., Rittman-Grauer, L., Biedler, J.L., Melamed, M.R., and Bertino, J.R. (1989). Multidrug-resistance gene (P-glycoprotein) is expressed by endothelial cells at blood-brain barrier sites. Proc. Natl. Acad. Sci. U S A *86*, 695–698.

Cucullo, L., Couraud, P.-O., Weksler, B., Romero, I.-A., Hossain, M., Rapp, E., and Janigro, D. (2008). Immortalized human brain endothelial cells and flow-based vascular modeling: a marriage of convenience for rational neurovascular studies. J. Cereb. Blood Flow Metab. *28*, 312–328.

Daneman, R., and Prat, A. (2015). The blood-brain barrier. Cold Spring Harb. Perspect. Biol. *7*, a020412.

Deo, A.K., Theil, F.-P., and Nicolas, J.-M. (2013). Confounding parameters in preclinical assessment of blood-brain barrier permeation: an overview with emphasis on species differences and effect of disease states. Mol. Pharm. *10*, 1581–1595.

DeStefano, J.G., Xu, Z.S., Williams, A.J., Yimam, N., and Searson, P.C. (2017). Effect of shear stress on iPSC-derived human brain microvascular endothelial cells (dhBMECs). Fluids Barriers CNS *14*, 20.

Galie, P.A., Nguyen, D.-H.T., Choi, C.K., Cohen, D.M., Janmey, P.A., and Chen, C.S. (2014). Fluid shear stress threshold regulates angiogenic sprouting. Proc. Natl. Acad. Sci. U S A *111*, 7968–7973.

Garcia-Polite, F., Martorell, J., Del Rey-Puech, P., Melgar-Lesmes, P., O'Brien, C.C., Roquer, J., Ois, A., Principe, A., Edelman, E.R., and Balcells, M. (2017). Pulsatility and high shear stress deteriorate barrier phenotype in brain microvascular endothelium. J. Cereb. Blood Flow Metab. *37*, 2614–2625.

Golden, A.P., and Tien, J. (2007). Fabrication of microfluidic hydrogels using molded gelatin as a sacrificial element. Lab Chip *7*, 720–725.

Helms, H.C., Abbott, N.J., Burek, M., Cecchelli, R., Couraud, P.-O., Deli, M.A., Förster, C., Galla, H.J., Romero, I.A., Shusta, E.V., et al.

(2016). In vitro models of the blood-brain barrier: an overview of commonly used brain endothelial cell culture models and guidelines for their use. J. Cereb. Blood Flow Metab. *36*, 862–890.

Hollmann, E.K., Bailey, A.K., Potharazu, A.V., Neely, M.D., Bowman, A.B., and Lippmann, E.S. (2017). Accelerated differentiation of human induced pluripotent stem cells to blood-brain barrier endothelial cells. Fluids Barriers CNS *14*, 9.

Huh, D., Hamilton, G.A., and Ingber, D.E. (2011). From 3D cell culture to organs-on-chips. Trends Cell Biol. *21*, 745–754.

Ingram, P.N., Hind, L.E., Jiminez-Torres, J.A., Huttenlocher, A., and Beebe, D.J. (2016). An accessible organotypic microvessel model using iPSC-derived endothelium. Adv. Healthc. Mater. *7*, 1700497.

Jiménez-Torres, J.A., Peery, S.L., Sung, K.E., and Beebe, D.J. (2016). LumeNEXT: a practical method to pattern luminal structures in ECM gels. Adv. Healthc. Mater. *5*, 198–204.

Katt, M.E., Xu, Z.S., Gerecht, S., and Searson, P.C. (2016). Human brain microvascular endothelial cells derived from the BC1 iPS cell line exhibit a blood-brain barrier phenotype. PLoS One *11*, e0152105.

Kim, S., Lee, H., Chung, M., and Li Jeon, N. (2013). Engineering of functional, perfusable 3D microvascular networks on a chip. Lab Chip *13*, 1489–1500.

Kluger, M.S., Clark, P.R., Tellides, G., Gerke, V., and Pober, J.S. (2013). Claudin-5 controls intercellular barriers of human dermal microvascular but not human umbilical vein endothelial cells. Arterioscler. Thromb. Vasc. Biol. *33*, 489–500.

Knowland, D., Arac, A., Sekiguchi, K.J., Hsu, M., Lutz, S.E., Perrino, J., Steinberg, G.K., Barres, B.A., Nimmerjahn, A., and Agalliu, D. (2014). Stepwise recruitment of transcellular and paracellular pathways underlies blood-brain barrier breakdown in stroke. Neuron *82*, 603–617.

Kolesky, D.B., Truby, R.L., Gladman, A.S., Busbee, T.A., Homan, K.A., and Lewis, J.A. (2014). 3D bioprinting of vascularized, heterogeneous cell-laden tissue constructs. Adv. Mater. *26*, 3124–3130.

Koutsiaris, A.G., Tachmitzi, S.V., and Batis, N. (2013). Wall shear stress quantification in the human conjunctival pre-capillary arterioles in vivo. Microvasc. Res. *85*, 34–39.

Kumar, K.K., Lowe, E.W., Aboud, A.A., Neely, M.D., Redha, R., Bauer, J.A., Odak, M., Weaver, C.D., Meiler, J., Aschner, M., et al. (2014). Cellular manganese content is developmentally regulated in human dopaminergic neurons. Sci. Rep. *4*, 6801.

Kutys, M.L., and Chen, C.S. (2016). Forces and mechanotransduction in 3D vascular biology. Curr. Opin. Cell Biol. *42*, 73–79.

Lee, J.B., Wang, X., Faley, S., Baer, B., Balikov, D.A., Sung, H.-J., and Bellan, L.M. (2016). Development of 3D microvascular networks within gelatin hydrogels using thermoresponsive sacrificial microfibers. Adv. Healthc. Mater. *5*, 781–785.

Lippmann, E.S., Azarin, S.M., Kay, J.E., Nessler, R.A., Wilson, H.K., Al-Ahmad, A., Palecek, S.P., and Shusta, E.V. (2012). Derivation of blood-brain barrier endothelial cells from human pluripotent stem cells. Nat. Biotechnol. *30*, 783–791.

Lippmann, E.S., Al-Ahmad, A., Azarin, S.M., Palecek, S.P., and Shusta, E.V. (2014). A retinoic acid-enhanced, multicellular human blood-brain barrier model derived from stem cell sources. Sci. Rep. *4*, 4160.

Markov, D.A., Lu, J.Q., Samson, P.C., Wikswo, J.P., and McCawley, L.J. (2012). Thick-tissue bioreactor as a platform for long-term organotypic culture and drug delivery. Lab Chip *12*, 4560–4568.

Miller, J.S., Stevens, K.R., Yang, M.T., Baker, B.M., Nguyen, D.-H.T., Cohen, D.M., Toro, E., Chen, A.A., Galie, P.A., Yu, X., et al. (2012). Rapid casting of patterned vascular networks for perfusable engineered three-dimensional tissues. Nat. Mater. *11*, 768–774.

Nitta, T., Hata, M., Gotoh, S., Seo, Y., Sasaki, H., Hashimoto, N., Furuse, M., and Tsukita, S. (2003). Size-selective loosening of the blood-brain barrier in claudin-5-deficient mice. J. Cell Biol. *161*, 653–660.

O'Grady, B., Wang, J., Faley, S., Balikov, D., Lippmann, E., and Bellan, L.M. (2018). A customizable, low-cost perfusion system for sustaining tissue constructs. SLAS Technol. *23*, 592–598.

Partyka, P.P., Godsey, G.A., Galie, J.R., Kosciuk, M.C., Acharya, N.K., Nagele, R.G., and Galie, P.A. (2017). Mechanical stress regulates transport in a compliant 3D model of the blood-brain barrier. Biomaterials *115*, 30–39.

Pellett, S., Schwartz, M.P., Tepp, W.H., Josephson, R., Scherf, J.M., Pier, C.L., Thomson, J.A., Murphy, W.L., and Johnson, E.A. (2015). Human induced pluripotent stem cell derived neuronal cells cultured on chemically-defined hydrogels for sensitive in vitro detection of Botulinum Neurotoxin. Sci. Rep. *5*, 14566.

Phan, D.T.T., Wang, X., Craver, B.M., Sobrino, A., Zhao, D., Chen, J.C., Lee, L.Y.N., George, S.C., Lee, A.P., and Hughes, C.C.W. (2017). A vascularized and perfused organ-on-a-chip platform for large-scale drug screening applications. Lab Chip *17*, 511–520.

Prabhakarpandian, B., Shen, M.-C., Nichols, J.B., Mills, I.R., Sidoryk-Wegrzynowicz, M., Aschner, M., and Pant, K. (2013). SyM-BBB: a microfluidic blood brain barrier model. Lab Chip *13*, 1093–1101.

Prasad, S., Sajja, R.K., Naik, P., and Cucullo, L. (2014). Diabetes mellitus and blood-brain barrier dysfunction: an overview. J. Pharmacovigil. *2*, 125.

Qian, T., Maguire, S.E., Canfield, S.G., Bao, X., Olson, W.R., Shusta, E.V., and Palecek, S.P. (2017). Directed differentiation of human pluripotent stem cells to blood-brain barrier endothelial cells. Sci. Adv. *3*, e1701679.

Ravi, M., Paramesh, V., Kaviya, S.R., Anuradha, E., and Solomon, F.D.P. (2015). 3D cell culture systems: advantages and applications. J. Cell. Physiol. *230*, 16–26.

Reinitz, A., DeStefano, J., Ye, M., Wong, A.D., and Searson, P.C. (2015). Human brain microvascular endothelial cells resist elongation due to shear stress. Microvasc. Res. *99*, 8–18.

Rochfort, K.D., Collins, L.E., McLoughlin, A., and Cummins, P.M. (2015). Shear-dependent attenuation of cellular ROS levels can suppress proinflammatory cytokine injury to human brain microvascular endothelial barrier properties. J. Cereb. Blood Flow Metab. *35*, 1648–1656.

Schindelin, J., Arganda-Carreras, I., Frise, E., Kaynig, V., Longair, M., Pietzsch, T., Preibisch, S., Rueden, C., Saalfeld, S., Schmid, B., et al. (2012). Fiji: an open-source platform for biological-image analysis. Nat. Methods *9*, 676–682.

Sweeney, M.D., Sagare, A.P., and Zlokovic, B.V. (2018). Blood-brain barrier breakdown in Alzheimer disease and other neurodegenerative disorders. Nat. Rev. Neurol. *14*, 133–150.

Tibbitt, M.W., and Anseth, K.S. (2009). Hydrogels as extracellular matrix mimics for 3D cell culture. Biotechnol. Bioeng. *103*, 655–663.

Wang, Y.I., Abaci, H.E., and Shuler, M.L. (2017). Microfluidic blood–brain barrier model provides in vivo-like barrier properties for drug permeability screening. Biotechnol. Bioeng. *114*, 184–194.

Weksler, B.B., Subileau, E.A., Perrière, N., Charneau, P., Holloway, K., Leveque, M., Tricoire-Leignel, H., Nicotra, A., Bourdoulous, S., Turowski, P., et al. (2005). Blood-brain barrier-specific properties of a human adult brain endothelial cell line. FASEB J. *19*, 1872–1874.

Wikswo, J.P. (2014). The relevance and potential roles of microphysiological systems in biology and medicine. Exp. Biol. Med. *239*, 1061–1072.

Wilson, H.K., Canfield, S.G., Hjortness, M.K., Palecek, S.P., and Shusta, E.V. (2015). Exploring the effects of cell seeding density on the differentiation of human pluripotent stem cells to brain microvascular endothelial cells. Fluids Barriers CNS *12*, 13.

Wilson, H.K., Faubion, M.G., Hjortness, M.K., Palecek, S.P., and Shusta, E.V. (2016). Cryopreservation of brain endothelial cells derived from human induced pluripotent stem cells is enhanced by rho-associated coiled coil-containing kinase inhibition. Tissue Eng. Part C Methods *22*, 1085–1094.

Ye, M., Sanchez, H.M., Hultz, M., Yang, Z., Bogorad, M., Wong, A.D., and Searson, P.C. (2014). Brain microvascular endothelial cells resist elongation due to curvature and shear stress. Sci. Rep. *4*, 4681.

Yu, J., Vodyanik, M.A., Smuga-Otto, K., Antosiewicz-Bourget, J., Frane, J.L., Tian, S., Nie, J., Jonsdottir, G.A., Ruotti, V., Stewart, R., et al. (2007). Induced pluripotent stem cell lines derived from human somatic cells. Science *318*, 1917–1920.

Zhang, Y., Sloan, S.A., Clarke, L.E., Caneda, C., Plaza, C.A., Blumenthal, P.D., Vogel, H., Steinberg, G.K., Edwards, M.S.B., Li, G., et al. (2016). Purification and characterization of progenitor and mature human astrocytes reveals transcriptional and functional differences with mouse. Neuron *89*, 37–53.

Zhang, J., Schwartz, M.P., Hou, Z., Bai, Y., Ardalani, H., Swanson, S., Steill, J., Ruotti, V., Elwell, A., Nguyen, B.K., et al. (2017). A genome-wide analysis of human pluripotent stem cell-derived endothelial cells in 2D or 3D culture. Stem Cell Reports *8*, 907–918.

Zheng, Y., Chen, J., Craven, M., Choi, N.W., Totorica, S., Diaz-Santana, A., Kermani, P., Hempstead, B., Fischbach-Teschl, C., López, J.A., et al. (2012). In vitro microvessels for the study of angiogenesis and thrombosis. Proc. Natl. Acad. Sci. U S A *109*, 9342–9347.

Stem Cell Reports, Volume *12*

Supplemental Information

iPSC-Derived Brain Endothelium Exhibits Stable, Long-Term Barrier Function in Perfused Hydrogel Scaffolds

Shannon L. Faley, Emma H. Neal, Jason X. Wang, Allison M. Bosworth, Callie M. Weber, Kylie M. Balotin, Ethan S. Lippmann, and Leon M. Bellan

Supplemental Figures

Figure S1. Effects of hydrogel composition upon EC attachment. Related to Figure 1.

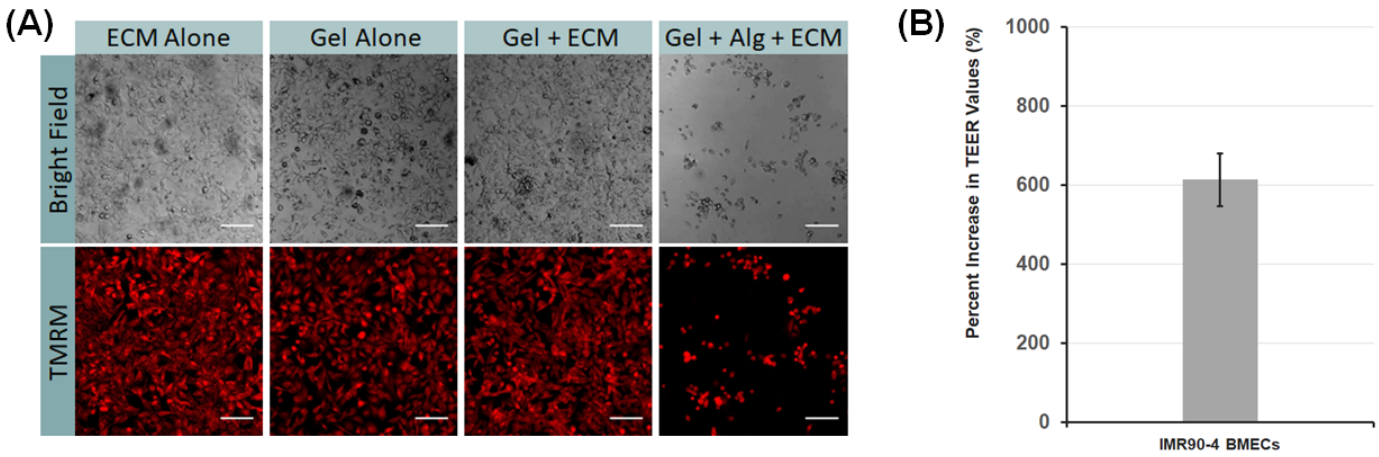

(A) IMR90-4-derived BMECs were seeded in 6-well plates coated with collagen/fibronectin solution (ECM Alone) or thin hydrogels comprised of enzymatically crosslinked 10% gelatin (Gel Alone), 10% gelatin treated with collagen/fibronectin (Gel + ECM), or 10% gelatin/0.25% Sodium-alginate treated with collagen/fibronectin solution (Gel+Alg+ECM). Gelatin/alginate hydrogels were crosslinked with mTG suspended in a 30 mM $CaCl_2$ solution. Cells were labeled with 1 µM mitochondrial stain, tertramethylrhodamineester (TMRM, Thermo Fisher) to identify live cells in fluorescence images. Scale bar represent 100 µm. **(B)** Graph illustrating the percent increase in maximum TEER values obtained from IMR90-4-derived BMECs, initially differentiated at starting iPSC densities of 120,000 or 150,000 cells per well (Hollmann et al., 2017), cultured on 7.5% gelatin hydrogels treated with collagen/fibronectin solution relative to non-treated hydrogels. Results reflects data compiled from 3 independent seedings from the 120,000 cells/well condition (N=3 Transwell filters per seeding, or N=9 total) and 2 independent seedings from the 150,000 cells/well condition (N=3 Transwell filters per seeding, or N=6 total). Error bars indicate ± 1 SD.

Figure S2. Permeability measurement data. Related to Figure 2.

(A)

Static Culture		Average	SD	*N1*	*N2*	*N3*
Day 1	IMR90-4 (D1)	1.22389E-07	5.9755E-08	1.6227E-07	5.4123E-08	1.5077E-07
	HUVEC	1.18354E-05	3.9553E-06	1.0857E-05	9.66E-06	1.499E-05
	uVas	4.95379E-07	3.6477E-07	2.7962E-07	2.9571E-07	9.1081E-07
Day 7	IMR90-4 (D1)	4.55303E-07	2.0771E-07	4.0714E-07	6.819E-07	2.7686E-07
	HUVEC	6.9814E-06	1.7915E-05	8.7731E-07	1.158E-06	1.8909E-05
	uVas	1.30489E-06	3.0378E-07	1.0538E-06	1.217E-06	1.6438E-06
Day 14	IMR90-4 (D2)	1.82649E-07	1.0749E-07	3.0547E-07	1.5376E-07	9.3933E-08
	IMR90-4 (D1)	2.15148E-06	3.6044E-06	1.8057E-07	4.1224E-06	3.1932E-06
	HUVEC	1.95006E-05	3.6499E-05	2.7554E-05	2.9059E-05	1.8894E-06
	uVas	1.23186E-06	2.1343E-07	1.2382E-06	1.017E-06	1.4438E-06
	CC3	1.98234E-07	1.019E-07	9.247E-08	2.9578E-07	2.0645E-07

(B)

Perfused Culture		Average	SD	*N1*	*N2*	*N3*
Day 1	IMR90-4 (D1)	1.94198E-07	1.8145E-08	2.0702E-07	1.8138E-07	1.8057E-07
	HUVEC	1.19041E-05	2.0004E-05	2.0793E-05	3.0155E-06	2.8306E-05
	uVas	5.95E-07	2.25E-07	5.30E-07	4.16E-07	7.56E-07
Day 7	IMR90-4 (D1)	1.40283E-07	8.6925E-08	9.3816E-08	2.4042E-07	8.6609E-08
	HUVEC	7.61697E-06	6.4097E-06	8.5993E-06	1.1918E-05	2.334E-06
	uVas	5.30E-07	1.04E-08	1.3171E-06	1.6912E-06	1.1606E-06
Day 14	IMR90-4 (D2)	3.21978E-09	1.733E-09	5.2198E-09	2.2743E-09	2.1652E-09
	IMR90-4 (D1)	4.27278E-08	3E-08	4.7624E-08	6.9907E-08	1.0653E-08
	HUVEC	2.28263E-05	1.1676E-05	1.8236E-05	2.2458E-05	2.7785E-05
	uVas	1.56426E-06	1.3679E-06	2.9212E-06	1.3171E-06	4.5456E-07
	CC3	4.24561E-08	2.7269E-08	2.5754E-08	2.7707E-08	7.3907E-08

Calculated values for 3 kDa dextran in **(A)** static and **(B)** perfused channels lined with HUVEC, μVas, IMR90-4-derived BMECs, or CC3-derived BMECs. Two explicitly different IMR90-4-derived BMEC batches were used to directly compare biological variance (denoted as D1 and D2).

Figure S3. qPCR analysis of BBB related markers. Related to Figure 2.

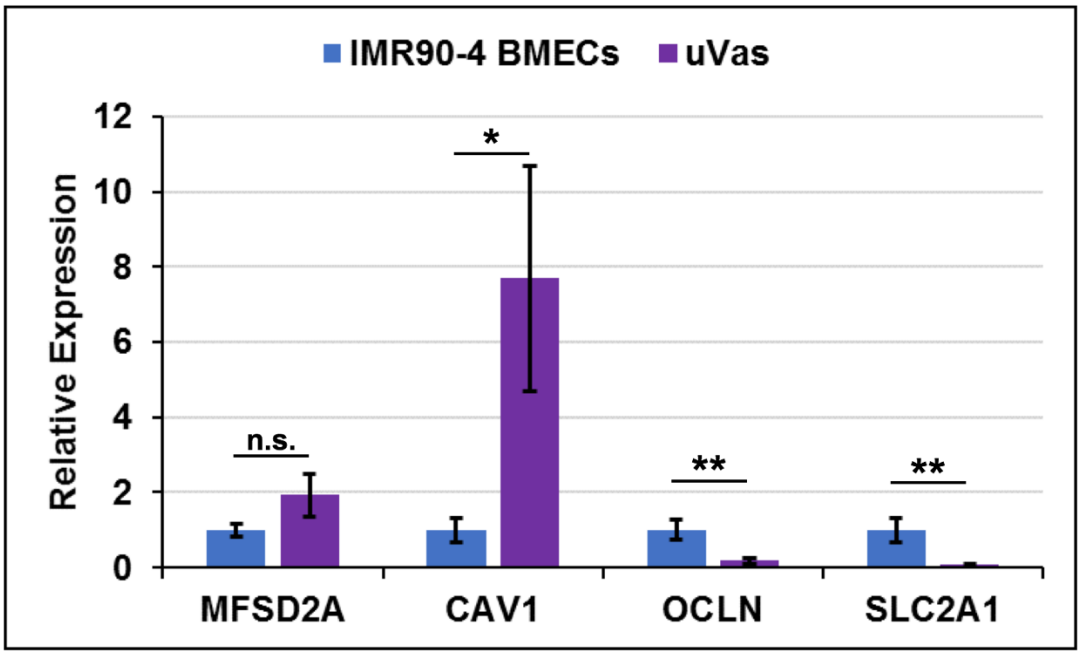

Relative expression of *MSFD2A*, *CAV1* (Caveolin-1), *OCLN* (Occludin), and *SLC2A1* (GLUT-1) in IMR90-4-derived BMECs versus μVas cells isolated from channels after 14 days of continual perfusion. *GAPDH* was used as the housekeeping gene. N=3 independent biological replicates for each condition. Error bars indicate ± 1 SD. Statistical significance was calculated using the student's unpaired t-test: *, $p<0.05$; **, $p<0.01$; n.s., $p>0.05$.

Figure S4. Permeability measurements from 3D stop-flow conditions and 2D Transwell controls. Related to Figure 2.

(A)

K (cm/s) (x10^{-7})		
Day 7	**BMEC**	6.4 ± 3.2
	HUVEC	114 ± 4.1
Day 14	**BMEC**	5.8 ± 2.2
	HUVEC	109 ± 15.4

(B)

K (cm/s) (x10^{-7})		
μVas	**Fluorescein**	507 ± 436
	3 kDa dextran	13.9 ± 2.7
	Albumin	0.03 ± 0.05
BMEC	**Fluorescein**	168 ± 50.8
	3 kDa dextran	102 ± 9.7
	Albumin	0.02 ± 0.001

(A) Permeability of CC3-derived BMECs and RFP-HUVECs to 3 kDa dextran when cultured on Transwell filters. **(B)** Permeability values from diffusion of sodium fluorescein, 3 kDa dextran, and albumin across cell monolayers after 14 days under stop-flow conditions. IMR90-4-derived BMECs and μVas were subjected to 10 min of media perfusion per day at 100 μl/min for 14 days. For all experiments, data represent mean ± SD calculated from N=3 independent biological replicates.

Figure S5. Perfusion system assembly components. Related to Figure 1.

(A)

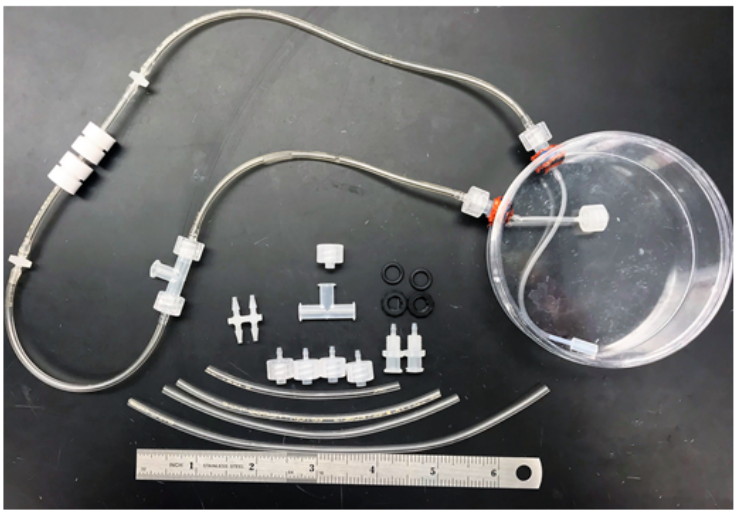

(B)

Materials	Volume
Tygon tubing - 1/16th in. (ID) x 22 in (L)	1.5 ml
Petri dish - 100 mm (D) x 30 mm (H)	40 ml
(4) 1/16th in. polypropylene Male barbed luer	
(2) 1/16th in. polypropylene barb to barb connector	
(2) Polypropylene 28 UNF threaded barb (1/16th in.) bulkhead	
(1) Polypropylene t-junction	
(1) Polypropylene luer cap	
(2) VIKON o-rings	
(2) PVDF bulkead locking nuts	

(A) Fully assembled fluidic culture apparatus used for continual and stop-flow perfusion experiments. **(B)** List of individual components used to construct perfusion system. The total volume of medium within the perfusion system during an experiment is estimated to be between 40-45 ml.

Figure S6. Measuring diffusion coefficients in gelatin matrix using FRAP analysis. Related to Figure 2 and Experimental Procedures.

(A.)

Diffusion Coefficient in 10% Gelatin (μ^2/s)	
Fluorescein (332 Da)	69.3 ± 1
3K Cascade Blue Dextran	22.5 ± 0.6
3K AF 680 Dextran	20.9 ± 0.3
10K Oregon Green Dextran	12.6 ± 0.5
Fluorescein-BSA (66K Da)	4.04 ± 0.3

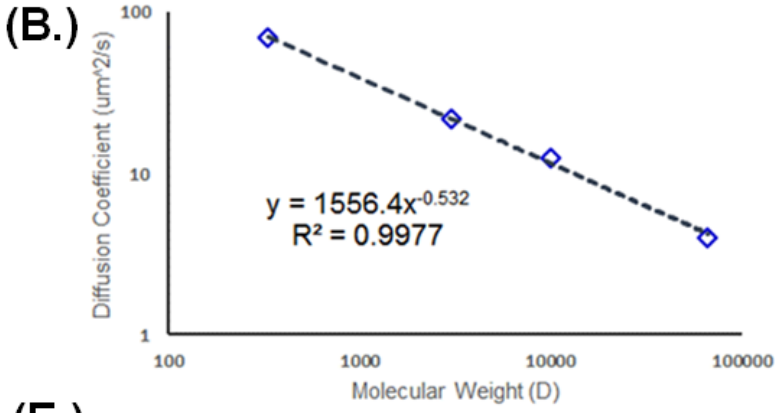

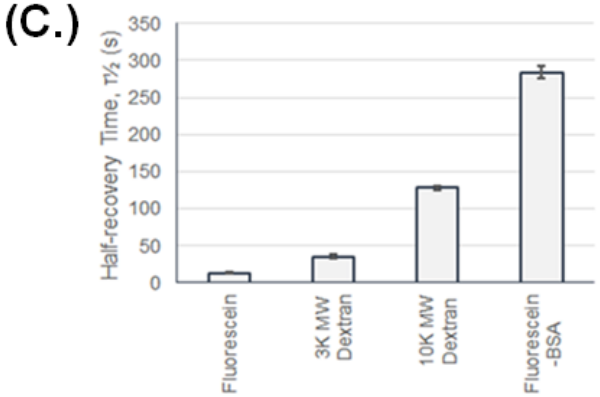

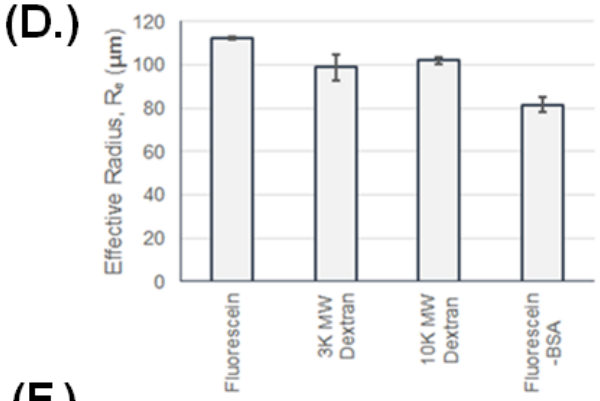

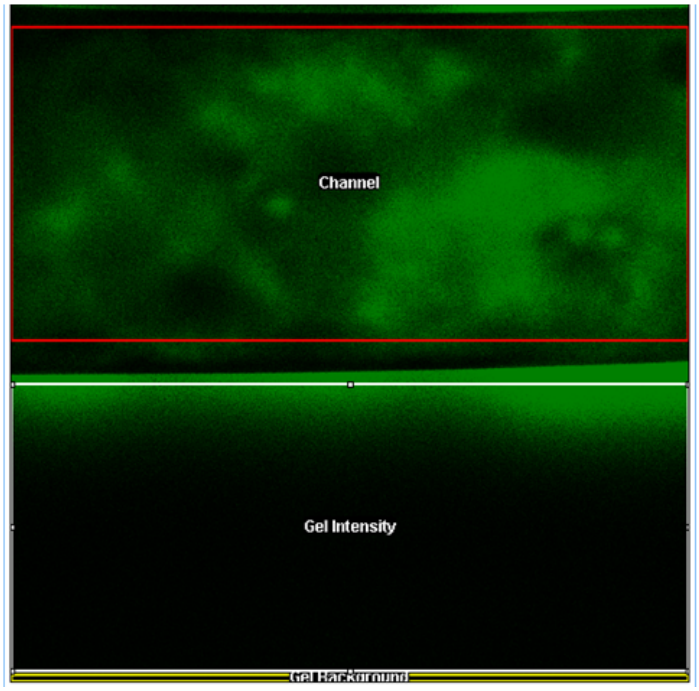

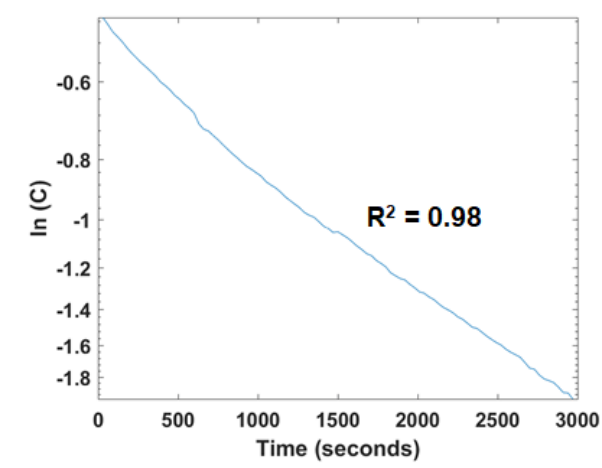

(A) Calculated diffusion coefficient values based upon N ≥ 3 experiments. **(B)** Comparison of molecular weight to calculated diffusion coefficient. Slope of the line is -0.53 with an R-squared value of 0.997, which correlates with previous reports (Arrio-Dupont et al., 1996). **(C)** Half-recovery times of fluorescein and dextran FRAP experiments. **(D)** Effective radius measurements of bleached samples. Error bars indicate ± 1 SD. **(E)** Screen capture illustrating ROI delineations for image processing in Fiji. **(F)** Representative plot of Log (C) versus time generated from intensity profiles in Matlab. The slope of the linear plot corresponds to Lambda (λ) and is used in Equation S4 to calculate the diffusion coefficient.

Supplemental Tables

Table S1. Global RNA expression in IMR90-4-derived BMECs cultured in channels for 1 day under static conditions and 14 days under perfused conditions. Related to Figure 2. Data are compiled in an accompanying spreadsheet.

Supplemental Movies

Movie 1. One-hour time-lapse showing diffusion of 3 kDa dextran across channels lined with RFP-HUVECs cultured under static conditions for 7 days. Related to Figure 2A.

Movie 2. One-hour time-lapse showing diffusion of 3 kDa dextran across channels lined with IMR90-4-derived BMECs cultured under static conditions for 7 days. Related to Figure 2A.

Movie 3. Two-hour time-lapse showing diffusion of fluorescein across channels lined with μVas cells cultured for 14 days under perfusion. Related to Figure 3A.

Movie 4. Two-hour time-lapse showing diffusion of fluorescein across channels lined with IMR90-4-derived BMECs cultured for 14 days under perfusion. Related to Figure 3A.

Supplemental Experimental Procedures

FRAP Measurements. In order to calculate the permeability of endothelial cell layers to sodium fluorescein, dextran, and albumin based upon time lapse images, the diffusivity of each molecule in gelatin was first determined through fluorescence recovery after photobleaching (FRAP) analysis. Excellent in-depth reviews of the principles and mathematical theory for determining diffusion coefficients based upon FRAP analysis have been previously described (Axelrod et al., 1976; Braeckmans et al., 2003; Soumpasis, 1983). In summary, an intense laser beam of known dimension is used to irreversibly bleach fluorophores within the exposed sample region. The diffusion coefficient is related to the speed at which the fluorescence the bleached region recovers, dictated by the speed at which bleached compounds diffuse out of the region and are replaced by unbleached fluorophores. Hence, the diffusion coefficient is most strongly related to the size of the compounds. Potential sources of error include immobilized compounds (e.g. molecules that stick to a coverslip) and unbound fluorophore which could under- or over-estimates of diffusion coefficients. To account for this, we performed FRAP analysis in control samples using five different compounds ranging in molecular weight between ~300 to 66,000 Daltons. Using multiple compounds of varying molecular weight allowed us to verify accuracy of the FRAP method as diffusivity should relate directly to molecular weight. Our results (**Figure S6**) indicated a strong linear relationship between diffusion coefficient and molecular weight, suggesting these potential sources error having minimal impact and, thus, no further steps to introduce correction for immobile molecules or unbound fluorophores were taken.

Uniform solutions of 10% (w/v) gelatin containing 10 μg/ml fluorescein (*MW = 332 g/mol*), 125 μg/ml Cascade Blue-Dextran (*MW = 3,000 g/mol*), 125 μg/ml Alexa-Fluor 680-Dextran (*MW = 3,000 g/mol*), 0.5 mg/ml Oregon Green-Dextran (*MW = 10,000 g/mol*), or 100 μg/ml Fluorescein-BSA (*MW = 66,000 g/mol*) were crosslinked with 1% (w/v) mTG. Approximately 200 μl of crosslinked gelatin solution containing individual fluorophores was sandwiched between two glass slides (Fisher Scientific) to form a thin gelatin layer approximately 60 μm in thickness. FRAP experiments were conducted using a Zeiss LSM 710 laser scanning confocal microscope and the bleaching module included in Zen Black (Zeiss) imaging software. For each trial, 10 pre-bleach images were obtained to calculate initial fluorescence intensity. Samples were then bleached, using the zoom-bleaching function to increase efficiency, with the appropriate laser (405 nm line of 30 mW Diode laser was used to bleach Cascade Blue Dextran, the 488 nm line of 35 mW Argon laser bleached Fluorescein, Oregon Green-Dextran, and Fluorescein-BSA, and 633 nm line of 5mW HeNe laser bleached Alexa-Fluor 680-Dextran) within a central designated bleach region (diameter = 60 pixels, or ~100 μm) until the bleached intensity reached 50% of the initial fluorescence intensity. Subsequent acquisition of time series images over the course of 100-500 seconds, depending on the dye, documented the fluorescence recovery. The pinhole aperture was held at maximum for all samples. Laser power was set to maximum to effectively bleach each dye through the entire thickness (*z*-axis) of the sample, such that fluorescence recovery depended most upon diffusion along the *x*-*y* dimension. To minimize the effects of diffusion occurring during the

process of photo-bleaching from skewing calculations based upon FRAP data, image resolution was set to 512x512 pixels per frame to reduce scan time (pixel dwell = 1.58 μs).

Calculating Diffusivity from FRAP Data. Diffusion coefficients for isotropic, nonreactive solutions were calculated from FRAP data based upon Fickian diffusion, most notably outlined by Axelrod and Soumpasis (Axelrod et al., 1976; Soumpasis, 1983) and later optimized (Braeckmans et al., 2003) to account for special consideration associated with photobleaching using laser-scanning confocal microscopy. Most recently, a simplified method for extracting the diffusion coefficients from confocal laser scanning FRAP data was described according to Equation S1, where D is the diffusion coefficient ($\mu m^2/s$), R_n is the nominal radius of the laser spot, R_e is the effective radius (1/2 diameter of bleached region), and $\tau_{1/2}$ is the half-recovery time (Kang et al., 2012).

$$\textbf{Equation (S1)}: \quad D = \frac{R_n^2 + R_e^2}{8\tau_{1/2}}$$

Automated measurements performed by modified version of the freely available Frap-jython macro for ImageJ (Schindelin et al., 2012; Schneider et al., 2012) provided the half-recovery time from individual FRAP data sets and identified the "FRAP frame" where fluorescence intensity within the bleached region reached a minimum. This frame was then used to measure the effective radius (R_e) from the plot profile function in ImageJ. The nominal radius (R_n) was the same for every sample at 50 μm. Calculated diffusion coefficients based upon FRAP experiments are shown in **Figure S6**.

Diffusion Imaging Analysis. Using Fiji, each dataset was first aligned (if necessary), before identifying the coordinates defining each region of interest corresponding to the areas comprising (1) channel interior, (2) gelatin background (farthest point from channel) and (3) gelatin next to the channel were entered into a custom Fiji macro. The macro script used to obtain the intensity profiles corresponding to the aforementioned region of interest is included as **Appendix S1**. Diffusivity was then calculated based on methods previously reported (Zheng et al., 2012), first using Equation S2:

$$\textbf{Equation (S2)}: Bi = \frac{K\delta}{D_{gelatin}} = \lambda \cdot tan\lambda$$

Where Bi is the Biot number, K (cm/s) is the permeability, δ is the distance between the edge of the channel and the edge of the gel (cm), $D_{gelatin}$ (cm/s) is the diffusivity of the compound of interest (e.g. 3 kDa dextran) in gelatin, and λ is the slope of linear fit for the following relation describing the change in fluorescence intensity versus time:

$$\textbf{Equation (S3)}: \lambda = \ln\left(\Delta \frac{I_{edge} - I_{channel}}{I_{gel} - I_{channel}}\right) \cdot \frac{1}{\Delta t}$$

Where I_{edge} is the integrated fluorescence intensity profile corresponding to the edge of the gelatin scaffold (also referenced as gel background), $I_{channel}$ is the integrated fluorescence intensity profile of channel, and I_{gel} correspond to the fluorescence

intensity of the gel next to the channel (the active area of dextran diffusion). The previous two equations are combined to yield a formula for determining permeability (K):

$$\textbf{Equation (S4)}: K = \frac{D_{gelatin} \cdot \lambda \cdot \tan \lambda}{\delta}$$

The intensity profiles extracted from imaging analysis were then imported into a Matlab script to calculate the permeability of cell layers to generate a plot corresponding to Equation S3, which was used to determine λ. This value was then used in Equation S4, along with known values for $D_{gelatin}$ and distance (δ) to calculate the permeability (K) reflecting the combined permeability of the gelatin matrix and cell monolayer. The Matlab script used for these calculations is included as **Appendix S2**.

Control scaffolds comprised of channels without cells lining the channel were used to determine the permeability of the gelatin matrix alone (K_g). The permeability of the cell monolayer (K_c) was then determined using the following equation:

$$\textbf{Equation (S5)}: \quad \frac{1}{k} = \frac{1}{k_C} + \frac{1}{k_G}$$

Shear Calculations. Fluidic shear stress along the channel wall using the following equations:

$$\textbf{Equation (S6)}: V = \frac{Q}{A}$$

Where V is the mean fluid velocity (mm/s), Q is the pump flow rate, and A is the area of the channel. An average channel diameter (d) of 800 μm was used for all calculations. We then calculated wall shear rate (γ) using:

$$\textbf{Equation (S7)}: \gamma = 8 * \frac{V}{d}$$

Shear stress (τ) is then calculated by:

$$\textbf{Equation (S7)}: \tau = \gamma * \mu$$

where μ is viscosity. For all calculations, the media viscosity was approximated using the viscosity for 1X PBS, 0.01 Pa (Yeom et al., 2014).

Immunocytochemistry. At indicated time points, gelatin constructs were washed 3 times in 1X PBS, then fixed in 4% paraformaldehyde for 10 min at room temperature (RT). Fixed constructs were washed 3 times in 1X PBS at RT, then incubated in 1X PBS supplemented with 5% donkey serum overnight at 4 °C. After washing with 1X PBS at RT, samples were incubated in 1X PBS containing 1 μg/ml claudin-5 antibody (Alexa-Fluor 488 conjugate; 4C3C2; Thermo Fisher), 1 μg/ml occludin antibody (Alexa-Fluor 594 conjugate; OC-3F10; Thermo Fisher), and/or 1 μg/ml VE-Cadherin antibody (PA519612, Thermo Fisher) overnight at 4 °C. Samples were washed 3 times in 1X PBS before incubation with 1 mg/ml Alexa-Fluor 680 donkey anti-rabbit secondary antibody (Thermo Fisher) overnight at 4 °C to fluorescently label bound VE-cadherin antibodies. Unbound secondary antibody was removed by washing 5 times in 1X PBS at RT. For actin labeling,

cells were incubated with Rhodamine Phalloidin (1:1000 dilution; Thermo Fisher) for 20 min at RT prior to imaging. For nuclei labeling, cells were incubated with 1 µg/ml Hoechst (BD Bioscience) for 10 min at RT prior to imaging.

qPCR Analysis. Cells were detached from the channel surface by first washing 2 times in 1X PBS for 5 min, then incubating the entire gel in 5 ml 0.25% Trypsin-EDTA (Gibco) at 37 °C for 10 min. Gels were then washed twice with 5 ml Trypsin Neutralizing solution (Gibco), vigorously pipetting the solution through the channels to dislodge remaining cells. Each collection tube included cells collected from two channels (experimental replicates). The cell suspensions were pelleted by centrifugation at 1000 G for 5 min. The supernatant was discarded and the pellet was resuspended in 500 µl of room temperature TRIzol reagent (Thermo Fisher) for 10 min before storage at -80 °C. To extract RNA, samples were mixed with chloroform at a 1:5 v/v chloroform:TRIzol and centrifuged at 12,000×g for 15 min at 4°C. RNA was subsequently isolated from the resulting aqueous phase and reversed transcribed to cDNA via manufacturers' instructions using an RNeasy Mini Kit (Qiagen) and a High-Capacity cDNA Reverse Transcription Kit (Applied Biosystems), respectively. qPCR was performed on a BioRad CFX96 using a TaqMan Universal PCR Master Mix (Applied Biosystems), 15 ng cDNA per replicate per gene, and desired TaqMan Gene Expression Assays (Applied Biosystems) and manufacturers' specified thermocycler parameters. Gene expression was measured using N=3 biological replicates.

RNA Sequencing and Analysis. IMR90-4-derived BMECs were detached from channels and collected in TRIzol as described above. Total RNA was isolated using the Direct-zol RNA MiniPrep Plus Kit (Zymo Research) with DNase I treatment according to the manufacturer's instructions. Samples were submitted to Vanderbilt Technologies for Advanced Genomics (VANTAGE) for sequencing using an Illumina NovaSeq6000. Sequences were aligned to the human transcriptome (GRCh38) using HISAT2 (Kim et al., 2015) and a text file containing a list of known splice sites generated using the UCSC Table Browser (Karolchik et al., 2004) and hisat2_extract_splice_sites.py. Alignments were assembled using StringTie (Pertea et al., 2015), and transcript levels (FPKM values) were extracted using Ballgown (Frazee et al., 2015). Pearson correlation coefficient was calculated by generating a scatter plot of FPKM values with each sample on a separate axis and performing a linear regression of the plotted data.

Supplemental References

Arrio-Dupont, M., Cribier, S., Foucault, G., Devaux, P.F., and d'Albis, A. (1996). Diffusion of fluorescently labeled macromolecules in cultured muscle cells. Biophys. J. *70*, 2327–2332.

Axelrod, D., Koppel, D.E., Schlessinger, J., Elson, E., and Webb, W.W. (1976). Mobility measurement by analysis of fluorescence photobleaching recovery kinetics. Biophys. J. *16*, 1055–1069.

Braeckmans, K., Peeters, L., Sanders, N.N., De Smedt, S.C., and Demeester, J. (2003). Three-dimensional fluorescence recovery after photobleaching with the confocal scanning laser microscope. Biophys. J. *85*, 2240–2252.

Frazee, A.C., Pertea, G., Jaffe, A.E., Langmead, B., Salzberg, S.L., and Leek, J.T. (2015). Ballgown bridges the gap between transcriptome assembly and expression analysis. Nat. Biotechnol. *33*, 243–246.

Hollmann, E.K., Bailey, A.K., Potharazu, A.V., Neely, M.D., Bowman, A.B., and Lippmann, E.S. (2017). Accelerated differentiation of human induced pluripotent stem cells to blood-brain barrier endothelial cells. Fluids Barriers CNS *14*, 9.

Kang, M., Day, C.A., Kenworthy, A.K., and DiBenedetto, E. (2012). Simplified equation to extract diffusion coefficients from confocal FRAP data. Traffic Cph. Den. *13*, 1589–1600.

Karolchik, D., Hinrichs, A.S., Furey, T.S., Roskin, K.M., Sugnet, C.W., Haussler, D., and Kent, W.J. (2004). The UCSC Table Browser data retrieval tool. Nucleic Acids Res. *32*, D493-496.

Kim, D., Langmead, B., and Salzberg, S.L. (2015). HISAT: a fast spliced aligner with low memory requirements. Nat. Methods *12*, 357–360.

Pertea, M., Pertea, G.M., Antonescu, C.M., Chang, T.-C., Mendell, J.T., and Salzberg, S.L. (2015). StringTie enables improved reconstruction of a transcriptome from RNA-seq reads. Nat. Biotechnol. *33*, 290–295.

Schindelin, J., Arganda-Carreras, I., Frise, E., Kaynig, V., Longair, M., Pietzsch, T., Preibisch, S., Rueden, C., Saalfeld, S., Schmid, B., et al. (2012). Fiji: an open-source platform for biological-image analysis. Nat. Methods *9*, 676–682.

Schneider, C.A., Rasband, W.S., and Eliceiri, K.W. (2012). NIH Image to ImageJ: 25 years of image analysis. Nat. Methods *9*, 671–675.

Soumpasis, D.M. (1983). Theoretical analysis of fluorescence photobleaching recovery experiments. Biophys. J. *41*, 95–97.

Yeom, E., Kang, Y.J., and Lee, S.-J. (2014). Changes in velocity profile according to blood viscosity in a microchannel. Biomicrofluidics *8*.

Zheng, Y., Chen, J., Craven, M., Choi, N.W., Totorica, S., Diaz-Santana, A., Kermani, P., Hempstead, B., Fischbach-Teschl, C., López, J.A., et al. (2012). In vitro microvessels for the study of angiogenesis and thrombosis. Proc. Natl. Acad. Sci. U. S. A. *109*, 9342–9347.

Appendix: Data Analysis Macro Scripts

Appendix S1. Fiji macro script

```
//Analyze confocal timelapse data sets for permeability measurements

        //Find Background Intensity of Gelatin
        makeRectangle (0,1020, 1024, 10);
                  // add roi (x, y, width, height)
        macro "Show Statistics" {
            if (nSlices>1) run("Clear Results");
                           getVoxelSize(w, h, d, unit);
                n = getSliceNumber();
                for (i=1; i<=nSlices; i++) {
                    setSlice(i);
                    getStatistics(area, mean, min, max, std);
                    row = nResults;
                    if (nSlices==1)
                        setResult("Area ("+unit+"^2)", row, area);
                        setResult("Mean ", row, mean);
                        setResult("Std ", row, std);
                        setResult("Min ", row, min);
                        setResult("Max ", row, max);
                  }
                setSlice(n);
                updateResults();
                saveAs("Results","path\\file.csv");

        //Find Intensity of Channel
        makeRectangle (0,100, 1024, 300);
                  //add roi (x,y,w,h)
        macro "Show Statistics" {
            if (nSlices>1) run("Clear Results");
                           getVoxelSize(w, h, d, unit);
                n = getSliceNumber();
                for (i=1; i<=nSlices; i++) {
                    setSlice(i);
                    getStatistics(area, mean, min, max, std);
                    row = nResults;
                    if (nSlices==1)
                        setResult("Area ("+unit+"^2)", row, area);
                        setResult("Mean ", row, mean);
                        setResult("Std ", row, std);
                        setResult("Min ", row, min);
                        setResult("Max ", row, max);
                  }
                setSlice(n);
                updateResults();
                saveAs("Results", "path\\name.csv");
                  }

        //Find Intensity of Gelatin near channel
        makeRectangle (0,450, 1024, 560);
                  // add roi (x, y, w,h)
        macro "Show Statistics" {
            if (nSlices>1) run("Clear Results");
                           getVoxelSize(w, h, d, unit);
                n = getSliceNumber();
                for (i=1; i<=nSlices; i++) {
                    setSlice(i);
                    getStatistics(area, mean, min, max, std);
                    row = nResults;
                    if (nSlices==1)
                        setResult("Area ("+unit+"^2)", row, area);
                        setResult("Mean ", row, mean);
                        setResult("Std ", row, std);
                        setResult("Min ", row, min);
                        setResult("Max ", row, max);
                  }
                setSlice(n);
                updateResults();
                saveAs("Results","path\\filename.csv");
        }

        //Analyze Time Series
        makeLine(0,512,1024,512,1);
                  //add line of interest
                  //(x1,y1,x2,y2,width)
        macro "Stack profile Data" {
            if (!(selectionType()==0 || selectionType==5 ||
        selectionType==6))
                exit("Line or Rectangle Selection Required");
                setBatchMode(true);
                  run("Plot Profile");
                  Plot.getValues(x, y);
                  run("Clear Results");
                  for (i=0; i<x.length; i++)
            setResult("x", i, x[i]);
                   close();
            n = nSlices;
                for (slice=1; slice<=n; slice++) {
                           showProgress(slice, n);
                           setSlice(slice);
                           profile = getProfile();
                           sliceLabel = toString(slice);
                           sliceData = split("\n");
                                   if (sliceData.length>0) {
                                           line0 = sliceData[0];
                                                   if
        (lengthOf(sliceLabel) > 0)

                  sliceLabel = sliceLabel+ " ("+ line0 + ")";
                  }
                           for (i=0; i<profile.length; i++)
                                   setResult(sliceLabel, i,
        profile[i]);
           }
                  setBatchMode(false);
                  updateResults;
                  saveAs("Results", "path\\filename.csv");
```

Appendix S2. Matlab code

```
%% Calculate permeability from confocal imaging datasets

    Dgelatin=20.9 %From FRAP Data 10k=12.6, 3k=20.9
    Distance_microns = 1120 %distance from channel edge to gel edge

    %%Import measurements from fiji macro
    Iedge = xlsread('C:\path\ GelBG.csv',1,'B2:B241');%%Average Intensity at no-flux region
    Channel_Io = xlsread('C:\pathChannelBG.csv',1,'B2:B241'); %%Intensity within channel
    Igel=  xlsread('C:\path\GelNearChannelBG.csv','B2:B241');%%Average intensity of gel

    %% Convert slice/frame number to time interval
    Slice = xlsread('C:\path\Profile.csv','Profile','C1:IH1');
    Time_minute = Slice*.5;
    Time_second = Time_minute*60;

    %%Calculating C for each timepoint
    C_numerator=Iedge-Channel_Io;
    C_denominator = Igel-Channel_Io;
    C=C_numerator./C_denominator;

    %% Graphing logC versus time
    x = Time_second;
    y = C;
    plot=semilogy(x,y);

    %%Fit logC versus time to extract Lambda (slope)
    curvefit = fitlm(x,y,'poly1');
        coeff=curvefit.Coefficients.Estimate;
        Rvalue=curvefit.Rsquared.Ordinary;
        output = xlswrite('C:\path\curvefit.xlsx', coeff,1);

    %Use Lambda to calculate K (permeability) in microns/second
    Lamda = xlsread('C:\path\curvefit.xlsx',1,'A2:A2');
    K=(Dgelatin/Distance_microns)*(Lamda*tan(Lamda));
    K_cm = K*10000; %% conversion to cm/s
        outputValue = {;'K cm/s';'Lambda';'Rsquared'}
        values=[;K_cm; K;Lamda;Rvalue];
        result= table(outputValue, values);
        %Save results in excel file
        writetable(result,'C:\path\Results.xlsx','Sheet',1,'Range','A1:B3')
```